Schweizerische Eidgenossenschaft
Confédération suisse
Confederazione Svizzera
Confederaziun svizra

Federal Department of the Environment, Transport, Energy and Communications DETEC

Swiss Federal Office of Energy SFOE
Energy Research and Cleantech Division

Final report dated 04.08.2022

Field monitoring of sediment transport, hydraulics and hydroabrasion at Swiss Sediment Bypass Tunnels

Felduntersuchung zu Hydraulik, Sedimenttransport und Hydroabrasion in Schweizer Sedimentumleitstollen

Source: © Romeo Arnold 2019

ETH zürich

Versuchsanstalt für Wasserbau,
Hydrologie und Glaziologie

Date: 04.08.2022

Location: Bern

Publisher:
Swiss Federal Office of Energy SFOE
Energy Research and Cleantech
CH-3003 Bern
www.bfe.admin.ch

Subsidy recipients:
ETH Zurich
Laboratory of Hydraulics, Hydrology and Glaviology (VAW)
Hönggerbergring 26
CH-8093 Zürich
www.vaw.ethz.ch

Authors:
Dr. Ismail Albayrak, ETH Zürich, albayrak@vaw.baug.ethz.ch
Romeo Arnold, ETH Zürich, arnold@vaw.baug.ethz.ch
Dr. Dila Demiral Yüzügüllü, ETH Zürich, demiral@vaw.baug.ethz.ch
Dr. Michelle Müller-Hagmann, ETH Zürich, michelle.mueller@runge-ag.ch
Prof. Dr. Robert Boes, ETH Zürich, boes@vaw.baug.ethz.ch

SFOE project coordinators:
Dr. Men Wirz, men.wirz@bfe.admin.ch
Dr. Klaus Jorde, klaus.jorde@kjconsult.net

SFOE contract number: SI/501609-01

The authors bear the entire responsibility for the content of this report and for the conclusions drawn therefrom.

Zusammenfassung

Speicher und Reservoire leisten einen wichtigen Beitrag zur Wasserkraftnutzung, werden aber durch Speicherverlandung mittel- bis langfristig beeinträchtigt. Sedimentumleitstollen (SBT) stellen eine effiziente Massnahme gegen die Speicherverlandung dar. Deren Wirtschaftlichkeit hängt von den hydraulischen und sedimentologischen Betriebsbedingungen sowie von der Abrasionsbeständigkeit der Auskleidungsmaterialien ab. Hydroabrasion ist ein allgegenwärtiges Problem, nicht nur bei SBT, sondern auch bei anderen wasserbaulichen Anlagen, die hohen Fliessgeschwindigkeiten und Sedimenttransportraten ausgesetzt sind. Das vorliegende Pilot- und Demonstrationsprojekt zielte daher darauf ab, das Verständnis der Abrasionsmechanik zu verbessern und ein mechanistisches Abrasionsmodell zu kalibrieren und zu verbessern, indem eine vierjährige Feldstudie an drei Schweizer SBTs durchgeführt wurde.

In diesem Projekt wurde die Abrasionsbeständigkeit verschiedener Sohlmaterialien durch jährliches 3D-Laserscanning quantifiziert, und die hydraulischen Bedingungen und der Sedimenttransport wurden zwischen 2017 und 2021 an den SBT Solis, Pfaffensprung und Runcahez in der Schweiz messtechnisch erfasst. Darüber hinaus wurde das am Auslauf des Solis SBT installierte *Swiss Plate Geophone System* (SPGS) im Jahr 2021 kalibriert und ein neuer Kalibrierungskoeffizient als Funktion des Partikeldurchmessers und des Partikelüberlappungsparameters z_p aus den aktuellen und früheren Kalibrierungsdaten bestimmt.

Die Ergebnisse zeigen, dass die Hydraulik der SBT-Strömung die Abrasionsmuster an den Tunnelwänden beeinflusst. Im geraden Abschnitt des Solis SBT, in dem das Längenverhältnis zwischen Tunnelbreite und Fließtiefe mit 1.7 weniger als 2 beträgt, konzentrieren sich Sedimenttransport und Hydroabrasion aufgrund der starken Sekundärströmungen auf die Tunnelmitte mit Maxima zwischen 110 % und 190 % der mittleren Abrasionstiefe über die gesamte Tunnelbreite. Wenn das Seitenverhältnis größer als 2 ist, wie im Runcahez SBT mit 2.375, konzentrieren sich der Sedimenttransport und die Hydroabrasion auf die Nähe zu den Tunnelwänden. Beim SBT Pfaffensprung hat die zweite Art von Sekundärströmungen aufgrund der Tunnelkrümmung zu einem hohen Sedimenttransport und einer starken Hydroabrasion auf der Innenseite der Krümmung und weiter tunnelabwärts, wo ein Beton-Testfeld installiert wurde, geführt. Bei den Granit- und Schmelzbasalt-Testfeldern in den SBT Pfaffensprung und Solis wurden höhere Abrasionstiefen an den Fugen festgestellt.

Granitplatten, Schmelzbasaltplatten und Stahlplatten sowie Kaliumaluminatzementbeton zeigen ein gutes Verhalten, um sedimenthaltigen Abflüssen und hydroabrasiven Prozessen in den SBT Solis und Pfaffensprung standzuhalten. Im SBT Runcahez zeigt der Stahlfaserbeton die beste Leistung. Der Abrasionswiderstand von Urner Granit ist etwa 7.5 Mal höher als der von hochfestem Beton im SBT Pfaffensprung.

Das mechanistische Abrasionsmodell, das in einer kürzlich abgeschlossenen experimentellen Laborforschung an der VAW verbessert wurde, wurde mit den vorliegenden Abrasion- und Sedimentdaten kalibriert, und es wurde ein Mittelwert des Abrasionskoeffizienten $k_v = (4.8 \pm 2.2) \times 10^4$ ermittelt. Dieses verbesserte Modell ist sowohl im Labor- als auch im Feldmaßstab anwendbar, z. B. für Wasserbauwerke und Flüsse auf steiler felsiger Sohle, was darauf hindeutet, dass die Laborergebnisse auf den Prototypmaßstab übertragen werden können. Die technische Anwendung des Modells wird vorgestellt.

Die Ergebnisse dieses Projekts sollen schliesslich zu einer nachhaltigen und wirtschaftlichen Nutzung wasserbaulicher Anlagen beitragen und den SBT-Betrieb hinsichtlich Stauraumentlandung optimieren. Darüber hinaus trägt es auch zur Umsetzung der Schweizer Energiestrategie 2050 bei, in der die Wasserkraft eine Schlüsselrolle bei der Elektrizitätsproduktion und -speicherung spielt.

Résumé

Les réservoirs permettent l'exploitation du potentiel hydroélectrique, mais sont exposés à la sédimentation à moyen et à long terme. Les galeries de dérivation des sédiments (SBT) sont une mesure efficace contre la sédimentation des réservoirs. Cependant, leur rentabilité dépend des conditions hydrauliques et sédimentologiques ainsi que de la résistance hydroabrasive du matériau de carénage. L'hydroabrasion est un problème omniprésent affectant non seulement les SBT, mais également des autres structures hydrauliques exposées aux charriages et aux vitesses d'écoulement élevées. Le présent projet pilote et de démonstration vise donc à faire progresser la compréhension de la mécanique de l'abrasion et à calibrer et améliorer un modèle mécaniste d'abrasion par saltation en menant une étude de terrain de quatre ans sur trois SBT suisses.

Dans ce projet, la résistance à l'abrasion de divers matériaux de radier a été quantifiée annuellement avec un scanner laser 3D, et les conditions hydrauliques et le transport de sédiments ont été surveillés entre 2017 et 2021 aux SBT de Solis, Pfaffensprung et Runcahez en Suisse. En outre, le système de plaques géophones suisses (SPGS) installé à la sortie du SBT de Solis a été étalonné en 2021 et un nouveau coefficient d'étalonnage en fonction du diamètre des particules et du paramètre de chevauchement des particules de z_p a été déterminé à partir des données de calibrage actuelles et précédentes.

Les résultats montrent que l'hydraulique des écoulements du SBT affecte les schémas d'abrasion au niveau du radier du tunnel. Dans la section droite du SBT de Solis où le rapport de la largeur du tunnel à la profondeur de l'écoulement est 1.7 et ainsi inférieur à 2, les matériaux charriés et l'hydroabrasion se concentrent au centre du tunnel avec des maxima entre 110 % et 190 % de la profondeur moyenne d'abrasion sur la largeur du tunnel en raison des forts courants secondaires. Lorsque ce rapport est supérieur à 2, comme dans le SBT de Runcahez avec 2.375, le charriage et l'hydroabrasion se concentrent vers les parois du tunnel. Au SBT de Pfaffensprung, le deuxième type de courants secondaires, en raison du coude du tunnel, a provoqué un transport important des matériaux charriés et une hydroabrasion profonde à l'intérieur du coude et plus en aval, là où un champ d'essai en béton a été installé. Aux champs d'essai en granit et en basalte coulé aux SBT de Pfaffensprung et de Solis, respectivement, des profondeurs d'abrasion plus élevées au niveau des joints ont été déterminées.

Les plaques de granit, basalte coulé et d'acier ainsi que le béton de ciment d'aluminate de potassium montrent une bonne performance pour résister au charriage et aux processus hydroabrasifs aux SBT Solis et Pfaffensprung. Au SBT Runcahez, le béton de fibres d'acier présente les meilleures performances. La résistance à l'abrasion du granit est environ 7.5 fois supérieure à celle du béton à haute résistance au SBT Pfaffensprung.

Les propriétés des sédiments telles que la forme et la composition minérale changent d'un bassin versant à l'autre. Les sédiments du bassin versant de Solis sont relativement mous avec une dureté Mohs globale comprise entre 3.5 et 3.7, tandis que les sédiments de Pfaffensprung et Runcahez sont plus durs avec des valeurs globales de 5.4-5.6 et 4.9-5.2, respectivement, sur l'échelle de dureté Mohs. De telles différences dans la dureté des sédiments affectent l'hydroabrasion de manière significative.

Le modèle mécaniste d'abrasion par saltation amélioré au VAW dans le cadre d'un projet de recherche récent au laboratoire a été calibré avec les présentes données d'abrasion et de sédiments et une valeur moyenne du coefficient d'abrasion $k_v = (4.8 \pm 2.2) \times 10^4$ a été déterminée. Ce modèle amélioré est applicable à la fois à l'échelle du laboratoire et à celle du terrain, par exemple pour les constructions hydrauliques et les rivières raides à substrat rocheux, ce qui indique que les résultats du laboratoire peuvent être transposés à l'échelle du prototype. L'application du modèle en ingénierie est également présentée.

Les résultats de ce projet contribueront à une utilisation durable des constructions hydrauliques et à l'amélioration des régimes d'exploitation des SBT en ce qui concerne la sédimentation et la durée de vie des réservoirs. En outre, il contribue également à la mise en œuvre de la Stratégie énergétique 2050 de la Suisse, dans laquelle l'hydroélectricité joue un rôle clé dans la production et le stockage de l'électricité.

Summary

Reservoirs allow making better use of the hydropower potential but are subject to sedimentation in the medium and long term. Sediment Bypass Tunnels (SBTs) are effective measures against reservoir sedimentation. However, their cost-effectiveness depends on hydraulic and sedimentological operating conditions as well as on the resistance of the invert against hydroabrasive wear. Hydroabrasion is an omnipresent issue not only at SBTs but also at other hydraulic structures exposed to high sediment loads and flow velocities. The present pilot and demonstration project therefore aims at advancing the understanding of abrasion mechanics and, calibrating and enhancing the mechanistic saltation abrasion model by conducting a 4-year field study at three Swiss SBTs.

In this project, the abrasion resistance of various invert materials was quantified by annual 3D laser scanning and hydraulic conditions and sediment transport were monitored between 2017 and 2021 at Solis, Pfaffensprung and Runcahez SBTs in Switzerland. In addition, a Swiss Plate Geophone System (SPGS) installed at the outlet of the Solis SBT was calibrated in 2021 and a new calibration coefficient as a function of particle diameter and particle overlapping parameter of z_p was determined from the present and previous calibration data.

The results show that the hydraulics of SBT flows affect abrasion patterns at the tunnel inverts. In the straight section of Solis SBT where the aspect ratio of tunnel width to flow depth amounts to 1,7 and is thus below 2, sediment transport and hydroabrasion concentrated at the centre of the tunnel with longitudinally averaged maxima between 110% and 190% of the mean abrasion depth across the tunnel width due to the strong secondary currents. When the aspect ratio is larger than 2 as in Runcahez SBT with 2.375, the sediment transport and hydroabrasion concentrate towards the tunnel walls. At Pfaffensprung SBT, the second type of secondary currents due to a tunnel bend has caused high sediment transport and deep hydroabrasion at the inner side of the bend and further downstream, where a concrete test field was installed. At the granite and cast-basalt test fields at Pfaffensprung and Solis SBTs, respectively, higher abrasion depths at the joints were determined.

Granite, cast basalt and steel plates as well as the potassium aluminate cement concrete show a good performance to withstand sediment-laden flows and hydroabrasive processes at Solis and Pfaffensprung SBTs. At Runcahez SBT, the steel fiber concrete shows the best performance. The abrasion resistance of granite is roughly 7.5 times higher than that of high-strength concrete at Pfaffensprung SBT.

Sediment properties such as shape and mineralogical composition change from catchment to catchment. Sediments in the Solis catchment are relatively soft with a bulk Mohs hardness of between 3.5 and 3.7, whereas sediments in Pfaffensprung and Runcahez are harder with bulk Mohs hardness values of 5.4-5.6 and 4.9-5.2, respectively. Such differences in sediment hardness affect hydroabrasion significantly.

A mechanistic saltation abrasion model enhanced at VAW in a recent laboratory research project was calibrated with the present abrasion and sediment data and a mean value of the abrasion coefficient $k_v = (4.8 \pm 2.2) \times 10^4$ was determined. This enhanced model is applicable for both the laboratory and field scales such as at hydraulic structures and in steep bedrock rivers indicating that the laboratory findings can be upscaled to the prototype scale. An engineering application of the model is presented.

The findings of this project will contribute to the sustainable use of hydraulic structures and improved SBT operation regimes with regard to desilting and reservoir lifetime. Moreover, it also contributes to

the implementation of Switzerland's Energy Strategy 2050, in which hydropower plays a key role in electricity generation and storage.

Main findings

- The layout and hydraulic conditions of an SBT affect hydroabrasion patterns on the tunnel invert.
- Bends of the SBT alignment cause secondary flows which can lead to concentration of sediment transport and hence stronger hydroabrasion at the inner side of a bend.
- In a straight section of a tunnel, when the aspect ratio of tunnel width to flow depth is less than 2, sediment transport and hydroabrasion concentrate at the centre of the tunnel due to strong secondary current effects. When the aspect ratio is larger than 2, sediment transport and thus hydroabrasion concentrate towards the tunnel walls, typically forming near-wall incision channels.
- Granite, cast basalt and steel plates as well as the potassium aluminate cement concrete have higher hydroabrasion resistance than various (other) types of concrete.
- The ratio of sediment hardness to invert material hardness affects hydroabrasion and this effect is included in the enhanced mechanistic abrasion model.
- The mechanistic saltation abrasion model was calibrated with the present abrasion, sediment, and hydraulic data.
- A constant calibration coefficient was obtained independent of sediment and invert material properties.
- The enhanced model is applicable for both the laboratory and field scales such as hydraulic structures and steep bedrock rivers
- A Swiss Plate Geophone System at Solis SBT was calibrated and a calibration coefficient as a function of particle size and particle impact overlapping was proposed.

Contents

Abbreviations

CB	Cast Basalt Plates
ewz	Zurich Electric Company (Elektrizitätswerk Der Stadt Zürich)
FOEN	Federal Office for the Environment
GSD	Grain Size Distribution
HAC	Potassium Aluminate Cement Concrete
HSC	Hight Strength Concrete
HPC	High Performance Concrete
HPP	Hydropower plant
GR	Canton of Grisons
LSC	Low Shrinkage Concrete
NC	Normal Concrete
PC	Polymer Concrete
RCC	Roller Compacted Concrete
SA	Steel Armouring
SAM	Saltation Abrasion Model developed by Sklar and Dietrich (2004)
SAMA	Saltation Abrasion Model developed by Auel et al. (2017b)
SAMD	Saltation Abrasion Model developed by Demiral-Yüzügüllü (2021)
SBB	Swiss Federal Railway
SBT	Sediment Bypass Tunnel
SC	Silica Fume Concrete
SF	Steel Fiber Concrete
SGC	Solis Geophone Calibration
SPGS	Swiss Plate Geophone System
TFB	Technik und Forschung im Betonbau AG
TLS	Terrestrial laser scanner
UHPC	Ultra-High Performance Fiber Concrete
UR	Canton of Uri
VAW	Laboratory of Hydraulics, Hydrology and Glaciology
XRD	X-Ray Diffractometer

1 Introduction

1.1 Background information and current situation

Reservoirs allow making better use of the hydropower potential, but are subject to sedimentation in the medium and long term (Morris and Fan, 1998). Sediment bypass tunnels (SBTs), which route sediments around a dam, are an effective measure against reservoir sedimentation (Figure 1a). A major problem affecting most SBTs is severe hydroabrasion of the tunnel invert due to high bedload transport rates and high flow velocities (Harada *et al.*, 1997; Sumi *et al.*, 2004; Auel and Boes, 2011). Invert abrasion can cause considerable refurbishment and maintenance costs affecting the cost-effectiveness of these facilities as well as endangering the sustainable and reliable energy and water supply. Moreover, invert abrasion may also impair the stability of the tunnel as shown in Figure 1b. Hence, abrasion prediction models are required for design life estimations, selection of adequate lining materials and cost-effectiveness analyses (Boes *et al.*, 2014). Although mechanistic abrasion prediction models exist, their applicability to the prototype scale has rarely been investigated. There is a lack of knowledge, resulting in a considerable model uncertainty.

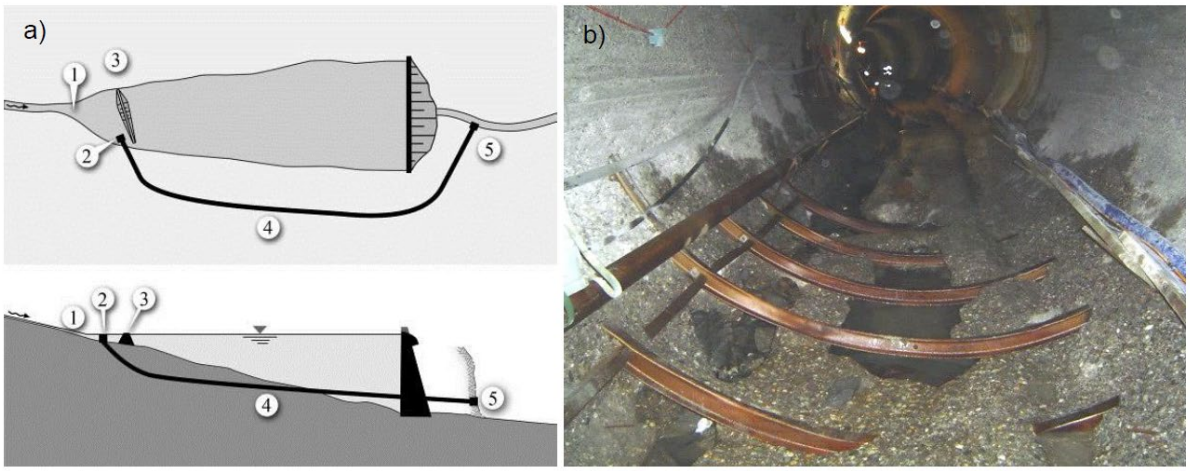

Figure 1: a) Sketch of a SBT with (1) reservoir head, (2) intake structure, (3) guiding structure, (4) tunnel, (5) outlet structure (VAW, ETH Zurich), b) exposed steel bearing due to hydroabrasion in SBT Val d'Ambra, Ticino, Switzerland (Müller-Hagmann 2017).

1.2 Purpose of the project

VAW of ETH Zurich has been investigating the hydroabrasion phenomenon at SBTs and at other hydraulic structures both in the laboratory and field by since 2011. At selected Swiss SBTs, bedload transport rates, hydraulic conditions and hydroabrasion were computed and monitored in the scope of a doctoral project (Müller-Hagmann, 2017), which was supported by BFE (SI/500731 and SI/501114). The monitoring included, amongst others, two 4-years (Solis and Pfaffensprung SBTs) and one 19-years field campaigns (Runcahez SBT). The latter based on an investigation conducted in the 1990s by VAW and TFB (Technik und Forschung im Betonbau AG) and hence enabled, to the authors' knowledge for the first time, a systematic long-term field investigation of hydroabrasion. The obtained data are of high interest especially for practical engineering application and reservoir sedimentation related research topics. The results showed that a widely used existing mechanistic abrasion model developed by Sklar and Dietrich (2004) and recently improved by Auel *et al*. (2017b) is suitable to estimate abrasion rates. However, the model's accuracy was shown to vary depending on the material and sediment properties (Auel *et al*., 2017b). Long-term field data are required to further improve and calibrate the model. To this end, the monitoring campaigns at the Swiss SBTs Solis (GR), Pfaffensprung (UR) and Runcahez (GR) were continued in the scope of the present project to obtain

the necessary data. The operators of these facilities showed continued interest in these investigations and supported the field campaigns.

1.3 Objectives

The goals of the present pilot project are to:

- extend the data base of hydroabrasive wear of various SBT inverts,
- contribute to the improvement of a state-of-the art abrasion prediction model,
- capture appreciable flood events and their impacts on the reservoirs,
- contribute to the optimization of design and operation of SBTs,
- provide a basis for improving sediment management at reservoirs,
- contribute to the realization of the Swiss Energy Strategy 2050 by increasing the efficiency of hydropower systems.

The project was led by VAW, ETH Zurich. The following operators supported the project along the field campaigns and make use of the obtained results:

- ewz, operator of the Solis SBT,
- SBB, operator of the Pfaffensprung SBT,
- Axpo Hydro, operator of the Runcahez SBT.

2 Description of facility and methodology

To reach the goals of the project, we monitored and determined (i) hydraulic operating conditions, (ii) sediment transport and (iii) hydroabrasive wear at Solis, Pfaffensprung and Runcahez SBTs. In addition, (iv) the properties of sediment collected from the catchments of these SBTs was analyzed with respect to its abrasive potential. Based on the obtained field data, a mechanistic abrasion model based on laboratory experiments was calibrated and extended to account for the abrasiveness of the sediment (Demiral-Yüzügüllü, 2021). In the following, the monitoring system and methodologies applied at the case study SBTs are described.

2.1 Solis SBT

The Solis reservoir is located in the Eastern Swiss Alps and was commissioned in 1986. It is fed by the Albula and by the tailrace water of the ewz-hydropower plant (HPP) Tiefencastel, which turbines water from the Julia River catchment. To reduce the sedimentation rates in the Solis reservoir and restore the interrupted sediment transport in the river reach, a one-kilometre long SBT was constructed and commissioned in 2012 (Figure 2).

The hydraulic operating conditions and sediment transport are continuously monitored at the Solis SBT. A Swiss Plate Geophone System (SPGS) assembled out of eight steel plates was installed at the outlet of the SBT to continuously monitor bedload transport (Figures 3 and 7). Although the SPGS was calibrated in the VAW laboratory in 2011 and 2013 and *in-situ* in 2016 (Albayrak *et al.*, 2017; Müller-Hagmann, 2017), additional *in-situ* tests with an enhanced procedure were conducted in 2021 to further reduce the uncertainty in bedload quantification (details of the calibration tests are presented in the following section 2.1.1). The SBT is equipped with six test fields F1 to F6 (4.4 x 10 m) made of different invert materials (see Table 1 and Table 20 for material properties). The test fields were scanned

regularly with a 3D laser scanner to determine the abrasion depths. In addition, the standard lining concrete just upstream (F0) and downstream of the test fields (F7) was also scanned.

Table 2 shows the used laser scanner and the corresponding measurement and registration errors. The registration error represents the error during the alignment process of different laser scan point clouds.

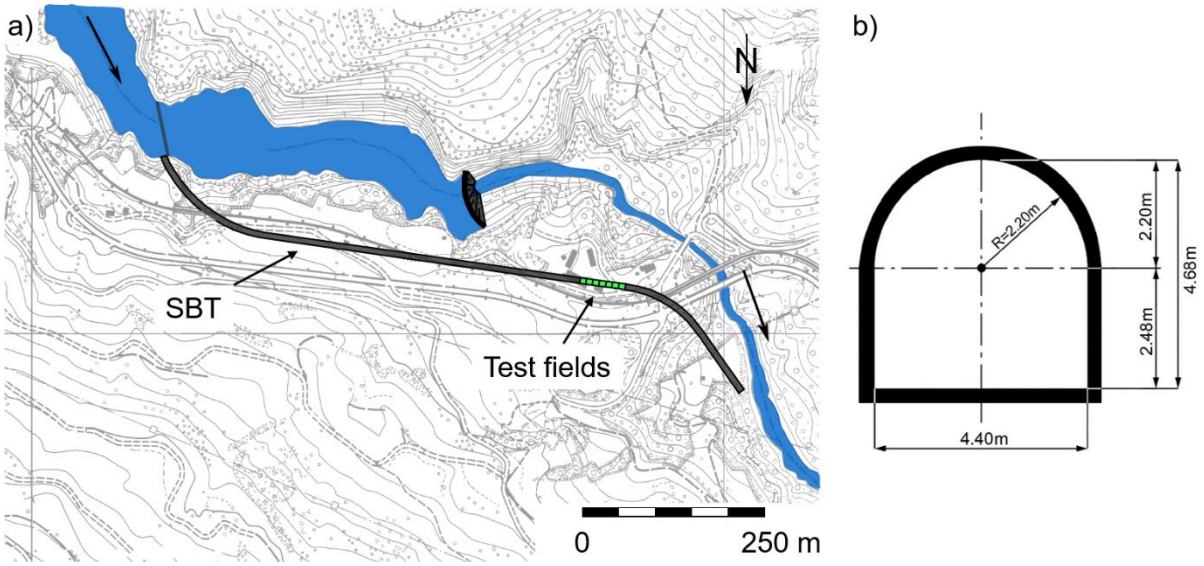

Figure 2: a) Plan view and b) cross section of Solis SBT (Müller-Hagmann, 2017).

Table 1: Test fields (with abbreviation) at Solis SBT with corresponding material specifications and producer (see Table 20 for material properties).

Test field	Material
F0 (NC)	Normal concrete (standard lining of SBT Solis)
F1 (HSC)	High-strength concrete with steel fibers (Albula)
F2 (LSC)	Low-shrinkage concrete with high modulus polymer fibers (Concretum)
F3 (HAC)	Potassium aluminate cement concrete (Hamitec)
F4 (UHPC)	Ultra-high performance fiber concrete (Holcim)
F5 (CB)	Cast basalt plates (Gerbas)
F6 (SA)	Steel armouring
F7 (NC)	Normal concrete (standard lining of SBT Solis)

Table 2: Used laser scanner and corresponding errors at Solis SBT.

Laser Scanner	Measuring error*	Registration error**
Leica ScanStation P15	0.5 - 1.0 mm at 20 m distance	2 mm

* According to data sheet of producer
** Error between scans of one measuring campaign

2.1.1 Geophone Field Calibration

The Swiss Plate Geophone System (SPGS) is a robust device allowing for continuous bedload transport monitoring in rivers and torrents with high flow velocities. The SPGS is submersible and consists of an elastically bedded steel plate mounted flush to the channel bed. The plate is equipped with a geophone sensor (GS-20DX, manufactured by “Geospace Technologies”, Houston, Texas, Fig. 3a), encased by a waterproof aluminium housing (Figure 3b). The length, width and thickness of the plate corresponding to streamwise, transversal and vertical directions are 36 cm, 50 cm, and 1.5 cm, respectively. The bearing between the steel plate and the mounting steel box is made of rubber. Besides signal damping issues, this bearing serves for isolating vibrational noise generated in the surroundings.

The sensor does not directly measure bedload transport, but records the vibration signal of the geophone plate, i.e., the vertical plate oscillations induced by impingement of passing sediment particles (Turowski *et al.*, 2013; Wyss, 2016). The signal output is a voltage corresponding to the plate velocity and is recorded at a sampling frequency of 10 kHz. To filter out background noise and vibrations generated by clear water flow, a threshold signal value of 0.1 V is defined in accordance with other applications (Rickenmann *et al*., 2013; Wyss, 2016; Chiari *et a*l., 2016). The threshold detection particle size amounts to d = 20 - 30 mm (Morach, 2011; Rickenmann *et al*., 2012; Wyss, 2016; Wyss *et al*., 2016a, b; Koshiba *et al*., 2018), below which particles might not be recorded any more. The number of impulses ‘Imp’ above the threshold value (Figure 3c) correlates linearly with bedload mass m (Rickenmann *et al*., 2012). The linear relation coefficient K_b between the number of impulses and bedload mass is used to estimate the sediment transport rate and is defined as:

$$K_b = \frac{Imp}{m} \qquad [1/kg] \qquad (1)$$

This calibration coefficient is affected by flow conditions, grain size and shape, and sediment transport rate. As adequate reproduction of these conditions in the laboratory is difficult, a site-specific calibration is required (Rickenmann *et al*., 2012, 2013; Wyss, 2016; Wyss *et al*., 2016a, b). The calibration coefficient is affected by signal interference induced by impact overlaps related to the sediment transport rate (Wyss, 2016; Dhont *et al*., 2017; Koshiba *et al*., 2018). The probability of this interference can be determined by z_p, defined as the ratio of total signal envelope time exceeding the impulse counting threshold (Figure 3c) to the total bedload sampling duration T (Wyss *et al*., 2015):

$$z_p = \frac{\sum \Delta t_i}{T} \qquad [1/kg] \qquad (2)$$

At $z_p \leq 0.01$, the signals of impinging particles rarely overlap and do not significantly affect the measurements, so that the bedload analysis is expected to deliver accurate results. However, with increasing z_p, the effect of signal overlaps increases and causes a certain signal saturation, biasing bedload estimations particularly for $z_p > 0.1$ (Wyss, 2016). Therefore, for accurate bedload estimation, a functional relationship between K_b and z_p needs to be established. To this end, at the latest geophone calibration campaign at Solis SBT in 2021, sediments were supplied to the tunnel at different transport rates causing different z_p values. On the contrary, for the geophone calibration conducted in the Solis SBT in 2016, the sediment transport rate was quasi-constant (Müller-Hagmann, 2017). Herein, the calibration tests in 2016 and 2021 are called ‘Solis Geophone Calibration 1 and 2 (SGC1 & SGC 2), respectively, and the results of the tests are compared in section 3.1.1.

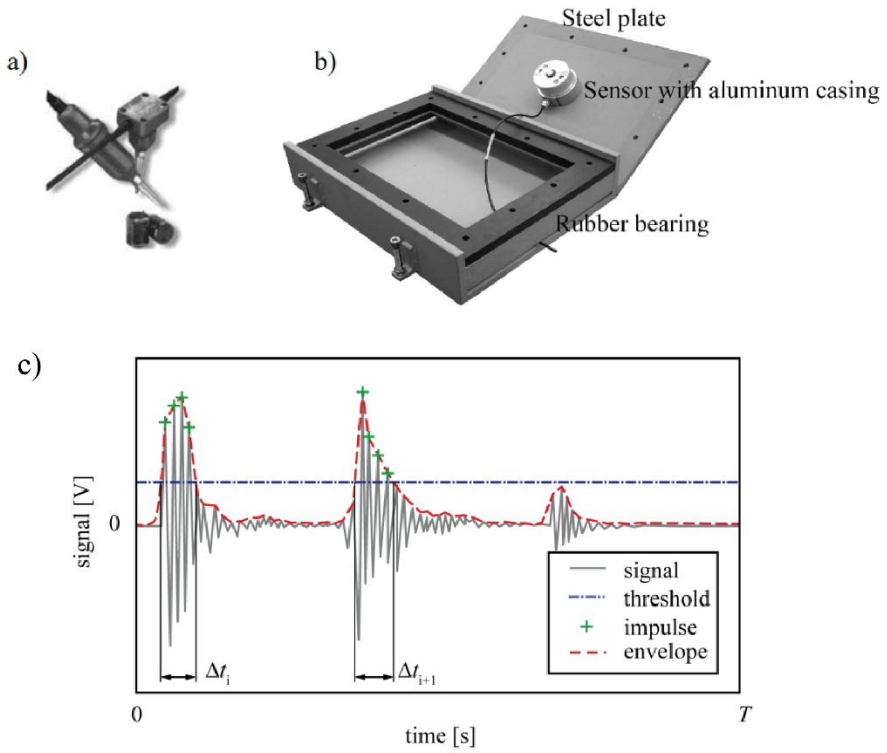

Figure 3: a) Geophone sensor (courtesy of Geospace Technologies), b) open measuring unit showing the steel plate and the waterproof aluminum casing of the sensor and c) Schematic geophone signal (Müller-Hagmann, 2017).

The SPGS installed at the outlet of the Solis SBT was calibrated *in-situ* using two different sediment size classes (16-32 mm & 32-63 mm, Figure 4) and different sediment transport rates in 2021 (SGC2). Four calibration runs, i.e., two different sediment transport rates for each size class, were conducted on 18 June 2021. The calibration procedure was as follows:

- the SBT was put in operation at high reservoir water level and SPGS signals were recorded for each run,
- the first 10 minutes of the recoded signals were under clear water conditions i.e., no sediment supply,
- after 10 minutes, sediments were supplied into the SBT via the shaft on the SBT ceiling near the SBT outlet using a truck mixer,
- the raw data of the SPGS were analysed.

All four test runs were conducted at identical flow condition listed in Table 3. Sediment parameters for each run are listed in Table 4. During the calibration, the sediment transport rate per unit tunnel width changed from 8.8 to 58.2 kg/(sm) resulting in z_p values from 0.015 to 0.090 averaged over 8 geophones from the recorded data (Table 4). The K_b values averaged over 8 geophones are between 9.44 and 21.81 1/kg. Both z_p and sediment size affect K_b values. A detailed analysis of the geophone data in comparison with the previous calibration data in 2016 (SGC1) is presented in subsection 3.1.1.

Table 3: Operating conditions in the SBT Solis during normal operation and field calibration in 2021.

	Normal operation	Field calibration in 2021
Q [m^3/s]	90 - 170	50
h [m]	2 - 3.6	1.16
U [m/s]	10.5 - 10.8	9.8
d [mm]	0 - 200	16 - 63

Table 4: Sediment parameters for each run during the field calibration in 2021.

Test run	Size class [mm]	d_m [mm]	Total mass [kg]	Duration [s]	Transport rate per unit width [kg/(sm)]	z_p [-]	K_b [1/kg]	Average K_b [1/kg]	Average z_p [-]
1	16-32	25	16390	1177	3.16	0.024	10.63	10	0.057
2	16-32	25	7960	133	13.60	0.090	9.44		
3	32-63	45	16770	510	7.47	0.087	18.68	20.24	0.051
4	32-63	45	7820	1842	0.96	0.015	21.81		

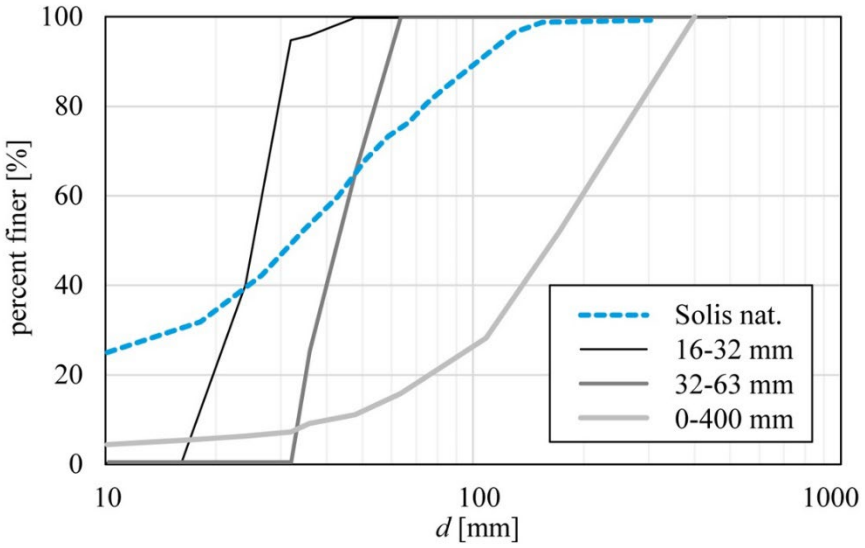

Figure 4: Sieve curves of the sediment samples of the calibration test of 2016 (SGC1) and the sediment in Solis reservoir (Müller-Hagmann, 2017).

2.2 Pfaffensprung SBT

The Pfaffensprung reservoir, impounding River Reuss, was built in 1922. The reservoir belongs to a cascade of three hydropower plants operated by the Swiss Federal Railways (SBB) and is located in Wassen, Canton of Uri, in the Central Swiss Alps. To avoid reservoir sedimentation, the reservoir has been equipped with a 282 m long SBT from the beginning (1922) (Figure 5). The tunnel cross section is a horse-shoe type. The tunnel has a longitudinal slope of 3%, except for the acceleration section at the inlet, where the slope is 35%. The hydraulic conditions at the Pfaffensprung SBT are continuously

measured and the data are regularly provided to VAW by the operator (SBB). Bedload transport was estimated by applying validated bedload transport formulas to the hydrographs of the Reuss. At the end of the SBT, two test fields (4.0 x 10 m) were implemented (see Table 5 and Table 20 for material properties). The test fields were scanned regularly with a 3D laser scanner to determine their abrasion depths between 2012 and the beginning of 2021.

Table 6 shows the used laser scanners and the corresponding errors. The registration errors represent the errors during the alignment process of different laser scan point clouds.

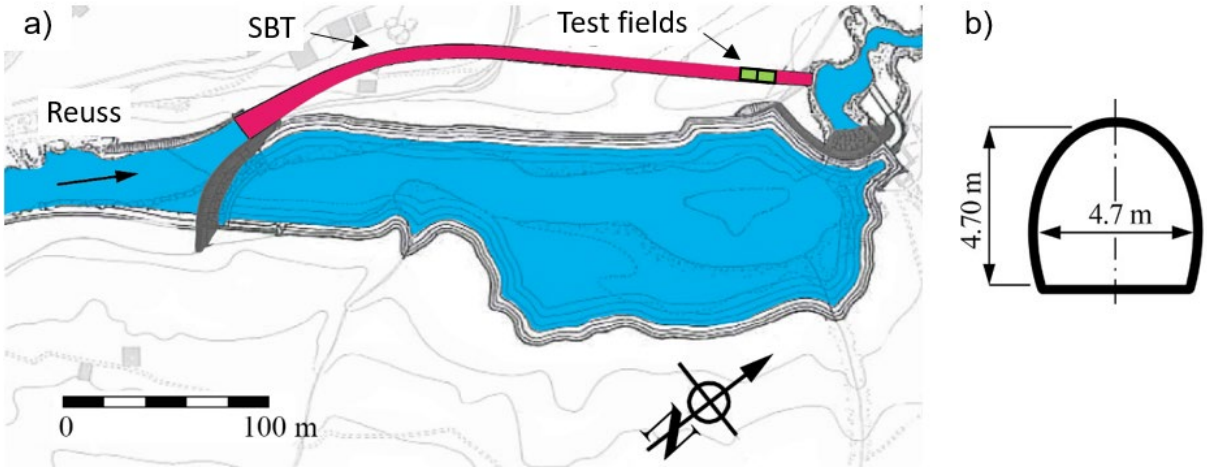

Figure 5: a) Plan view and b) cross section of Pfaffensprung SBT (Müller-Hagmann, 2017).

Table 5: Test fields (with abbreviation) at Pfaffensprung SBT with corresponding material specifications (see Table 20 for material properties).

Test field	Material
F1 (C)	High-strength concrete
F2 (G)	Granite paving (standard lining of SBT Pfaffensprung)

Table 6: Used laser scanners and corresponding errors at Pfaffensprung SBT.

Year	Laser Scanner	Measuring error*	Registration error A**	Registration error B**
2012	Z + F Imager 5006h	0.7 - 2.6 mm at 25 m distance	2 mm	2 - 3 mm
2017 - 2020	Leica ScanStation P15	0.5 - 1.0 mm at 20 m distance	1 - 2 mm	

* According to data sheet of producer

** Registration error A: error between scans of one measuring campaign
Registration error B: error between two measuring campaigns (scan of 2012 is always the basis)

2.3 Runcahez SBT

The Runcahez dam was commissioned in 1962 and its reservoir serves as a compensation basin between the hydropower plants Sedrun and Tavanasa of the Vorderrhein power cascade located in the Eastern Alps of Switzerland. To prevent reservoir sedimentation, a 572 m long SBT was constructed and put in operation in 1962 (Figure 6a). Its cross section is archway-shaped, 3.8 m wide

and 4.27 m high (Figure 6b). In this SBT, supercritical flow conditions occur, and the mean flow velocities vary between 5 and 16 m/s, depending on discharge.

Since no discharge data is available from the Runcahez SBT, the hydraulic conditions in the SBT are determined based on the hydrograph from the gauging station number 2430 (Rein da Sumvitg, Encardens) located 3.5 km upstream and managed by the Federal Office for the Environment (FOEN). The hydrograph is adapted according to the discharge relation of the FOEN gauging station and the SBT, which was determined based on the measurements conducted during flood events between 1996 and 1999. Bedload transport is estimated by applying a validated bedload transport formula to the hydrographs. The SBT is equipped with five test fields (3.8 x 10 m) (see Table 7 and Table 20 for material properties), which are scanned with a 3D laser scanner at the beginning and the end of the project duration to determine the abrasion depths. The SBT inlet lining was initially made of concrete, while in the downstream tunnel section, the invert is formed by bare rock. Different invert refurbishments were conducted over time using basalt plates and standard concrete.

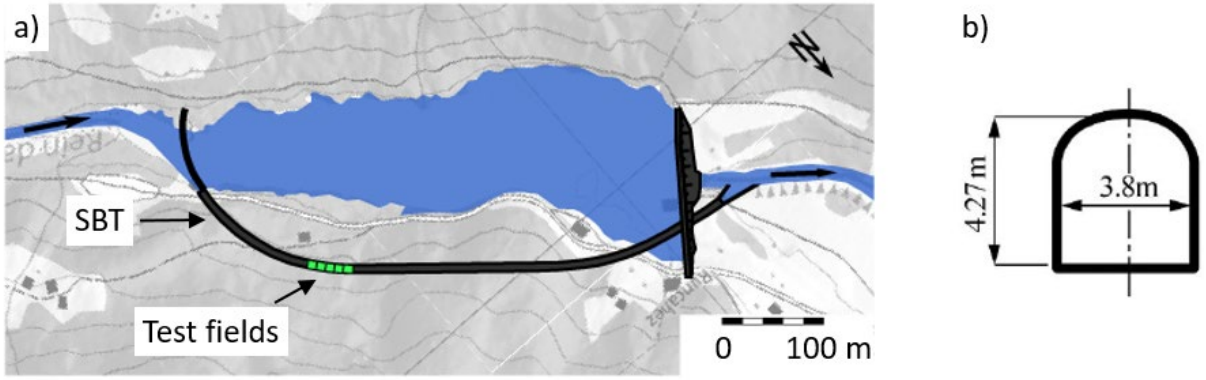

Figure 6: a) Plan view and b) cross section of Runcahez SBT (adapted from Jacobs et al., 2001).

Table 7: Test fields (with abbreviations) at Runcahez SBT with corresponding material specifications (see Table 20 for material properties).

Test field	Material
F1 (SC)	Silica fume concrete
F2 (RCC)	Roller compacted concrete
F3 (HPC)	High-performance concrete
F4 (SF)	Steel fiber concrete
F5 (PC)	Polymer concrete

2.4 Sediment properties in Solis, Pfaffensprung and Runcahez SBT

The abrasive potential of the sediment, depending on particle shape and hardness, is of prime importance for abrasion prediction and the selection of invert material. Therefore, sediments were sampled from the SBT catchments in summer 2019, in the river reaches either upstream or downstream of the respective SBT. The particle shapes were evaluated based on a common classification provided by ISO (2013). The mineralogical composition of the sediments was determined using an X-ray-diffractometer (XRD). The hardness of the sediment is assigned based on the mineralogy using tables from petrographic literature. The Mohs scale, a non-linear rather qualitative scale, is commonly used in this context (Felix, 2017). The scale ranges from 1 (chalk) to 10 (diamond). High fractions of hard particles, e.g., of feldspar and quartz (Mohs hardness 6 and 7, respectively) are

typical for igneous rocks, whereas sedimentary rocks are generally softer. Although the Mohs hardness scale is non-linear, the bulk hardness (= weighted average of the minerals' hardnesses) is used herein as a first approach since Xie and Tamaki (2007) revealed that the wear rate observed at machining processes such as drilling, sawing and grinding increases with the bulk hardness of granite. Finally, the result of this study, in combination with the results of physical scale model experiments conducted in a parallel PhD thesis at VAW by Demiral Yüzügüllü (2021) contribute to enhance existing abrasion models by adding a term accounting for the abrasive potential of the bypassed sediments.

2.5 Mechanistic hydroabrasion prediction model

Sklar and Dietrich (2004) developed a mechanistic hydroabrasion model (SAM), which enables to predict vertical abrasion rates based on the bed lining material properties, particle saltation trajectories, sediment supply rate, and sediment transport capacity. In a closed form, the SAM follows as (Sklar and Dietrich, 2004):

$$A_r = \frac{Y_M}{k_v f_{st}^2} \frac{W_{im}^2}{L_p} q_s p_o \qquad \text{[m/s]} \qquad (3)$$

where A_r = vertical abrasion rate [m/s], Y_M = Young's modulus of the bed lining material [Pa], f_{st} = splitting tensile strength of the bed lining material [Pa], k_v = abrasion resistance coefficient [-], W_{im} = vertical particle impact velocity [m/s], L_p = particle hop length [m], q_s = specific gravimetric sediment supply rate n [kg/(ms)], and p_o = cover effect term [-].

Auel (2014) and Auel *et al*. (2014, 2017a, 2017b) investigated the flow characteristics, saltation trajectories and particle impact of single grains in various supercritical open channel flow conditions over a fixed bed in transitionally rough regime. They modified the SAM by using newly developed formulae for the hop length and vertical particle impact velocity and proposed the following equation (SAMA, Auel *et al*., 2017b):

$$A_r = \frac{Y_M}{k_v f_{st}^2} \frac{(T^*)^{0.78}(s-1)g}{230(T^*)^{0.8}} q_s \left(1 - \frac{q_s}{q_s^*}\right) \qquad \text{[m/s]} \qquad (4)$$

$$T^* = \frac{\theta}{\theta_c} - 1 \qquad \text{[-]} \qquad (5)$$

$$\theta = \frac{U_*^2}{gD(s-1)} \qquad \text{[-]} \qquad (6)$$

where T^* = excess transport stage [-], θ = Shields parameter [-], θ_c = critical Shields parameter [-], U_* = friction velocity [m/s], D = particle diameter [m], $s = \rho_s/\rho$ = relative sediment density [-], ρ_s = sediment density [kg/m^3], ρ = water density [kg/m^3] and q_s^* = specific gravimetric sediment transport capacity [kg/(ms)]. The abrasion or rock resistance coefficient k_v relates the bed lining material resistance to hydroabrasive wear and is a key parameter in the abrasion prediction models. Sklar and Dietrich (2004) calibrated the k_v coefficient based on their abrasion mill data (Sklar & Dietrich, 2001), and the data obtained from particle drop tests (Sklar and Dietrich, 2004). The value of k_v varies in a range of $9.4 \times 10^5 \leq k_v \leq 9.1 \times 10^6$ (Sklar & Dietrich, 2012). Sklar and Dietrich (2012) proposed $k_v = 3.3 \times 10^6$ for different bedrock such as sandstone, limestone, andesite, graywacke, welded tuff, quartz, and concrete-like materials (mortars of different strengths) supporting the theory of constant k_v (Engel, 1978) although it varies around one order of magnitude.

Auel *et al*. (2017b) calibrated the k_v values for their SAMA model (Eq. 4). The $k_v \approx 10^5$ of SAMA for $f_{st} >$ 1 MPa is one order of magnitude lower compared to the value proposed by Sklar and Dietrich (2004, 2012). The difference between the abrasion resistance coefficients calculated by SAM and SAMA can be explained by the different equations developed for the vertical particle impact velocity and hop length. The k_v value of SAMA increases with increasing splitting tensile strength, revealing that the assumption of a constant k_v value is hardly valid for $f_{st} <$ 1 MPa. In a later study, Müller-Hagmann *et al*.

(2020) calibrated the model using the field data from Pfaffensrpung and Runcahez SBTs and their results confirm the findings of Auel *et al*., (2017b).

Recently, Demiral-Yüzügüllü (2021) investigated hydroabrasion mechanics in a laboratory flume by conducting velocity and particle motion measurements and hydroabrasion tests of various invert material. Her enhanced model is called 'SAMD' and was calibrated by her laboratory and literature data.

The SAMD model uses the following particle saltation probability, hop length, and vertical impact velocity formulae developed for the hydraulically rough bed:

$$P_S = 1 - P_R = 1 - 1.05(T^*)^{-0.90}, \quad 0 \le P_S \le 1, \quad \text{where } T^* > 1.05 \qquad [-] \qquad (7)$$

$$\frac{L_p}{D} = 10.1(T^*)^{0.75} \qquad [-] \qquad (8)$$

$$\frac{W_{im}}{[(s-1)gD]^{0.5}} = 0.30(T^*)^{0.34} \qquad [-] \qquad (9)$$

where P_s = particle saltation probability [-] and P_R = particle rolling probability [-]. SAMD includes the following equations for the particle hardness effect on hydroabrasion:

$$k_H = \begin{cases} \left(\frac{MH}{MH_B}\right)^{1.3}, & 1 \le \frac{MH}{MH_B} \le 2.3 \\ \left(\frac{MH}{MH_B}\right)^{0.3}, & \frac{MH}{MH_B} < 1 \end{cases} \qquad [-] \qquad (10)$$

where k_H = newly introduced non-dimensional hardness coefficient, MH = abrasive particle (sediment) Mohs hardness, and MH_B = bed lining material's Mohs hardness. The following exponential cover term is proposed for SAMD as a best representative of Demiral-Yüzügüllü's test results:

$$p_o = \begin{cases} \exp\left(-\varphi \frac{q_s}{q_s^*}\right), & q_s < q_s^* \\ 0, & q_s \ge q_s^* \end{cases} \qquad [-] \qquad (11)$$

In Eq.(11), φ = dimensionless cover factor, which is set to 1 to simplify the equation, and q_s^* = sediment transport capacity, which is calculated using the formula below:

$$q_s^* = 24(\theta - \theta_c)^{1.5} \rho_s [(s-1)gD^3]^{0.5} \qquad [\text{kg/(m·s)}] \qquad (12)$$

For fixed beds in hydraulically rough regime, the critical Shields parameter was found as θ_c = 0.013 (Demiral Yüzügüllü, 2021).

By including the new terms [Eqs.(7)], the enhanced mechanistic saltation abrasion model (SAMD) is written as follows in a closed form:

$$A_r = \frac{Y_M}{k_v f_{st}^2} k_H q_S P_S \frac{W_{im}^2}{L_p} p_o \qquad [\text{m/s}] \qquad (13)$$

SAMD follows in extended form as:

$$A_r = \begin{cases} \dfrac{Y_M}{k_v f_{st}^2}\left(\dfrac{MH}{MH_B}\right)^{1.3}\left[1-1.05(T^*)^{-0.90}\right]\dfrac{g(s-1)}{112}(T^*)^{-0.07} q_s \exp\left(-\dfrac{q_s}{q_s^*}\right), & q_s < q_s^* \text{ and } 1 \le \dfrac{MH}{MH_B} \le 2.3 \\ \dfrac{Y_M}{k_v f_{st}^2}\left(\dfrac{MH}{MH_B}\right)^{0.3}\left[1-1.05(T^*)^{-0.90}\right]\dfrac{g(s-1)}{112}(T^*)^{-0.07} q_s \exp\left(-\dfrac{q_s}{q_s^*}\right), & q_s < q_s^* \text{ and } \dfrac{MH}{MH_B} < 1 \\ 0 & , q_s \ge q_s^* \end{cases}$$

[m/s] (14)

The SAMD model was calibrated based on the present data obtained from the three Swiss SBTs, see section 4.

3 Results and discussion

3.1 Solis SBT

3.1.1 Geophone calibration

During the field calibration tests in 2021, herein called ‘Solis Geophone Calibration 2 (SGC2), significant concentrations of bed load transport on the right side of the tunnel were observed and confirmed by the geophone measurements (Figure 7a and b). This indicates the pronounced effects of the upstream tunnel curve on the lateral distribution of bedload transport. The sediment concentrations are comparable to those in normal SBT operation and confirm that realistic transport characteristics could be reproduced in the calibration tests. Similar results were obtained from the calibration tests in 2016 (herein called ‘SGC1’, Müller-Hagmann, 2017).

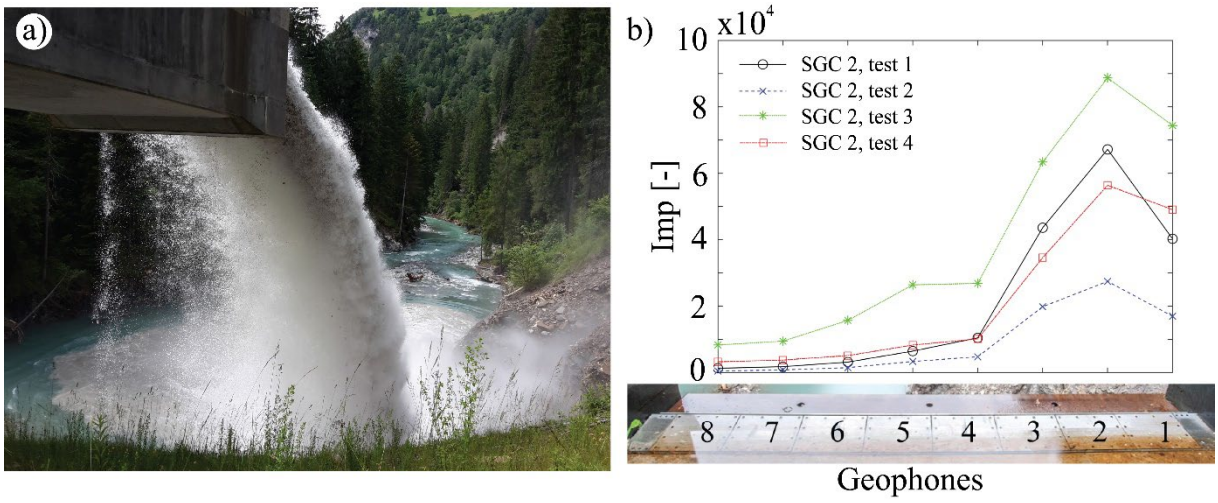

Figure 7: (a) Bed load transport concentration on the right-hand side at the discharge of the SBT Solis during a field calibration test, (b) Lateral distribution of bed load transport during the four field calibration tests in 2021.

Figure 8 shows the z_p values as a function of unit sediment transport rates q_s for both field calibrations at Solis SBT (SGC 1 and 2), laboratory tests of the geophone with a 10° inclination as in Solis SBT (Müller-Hagmann, 2017) and field tests with 0° geophone inclination by Wyss (2016). Based on the distribution of the number of particle impacts between eight geophones, shown in Figure 7, the

sediment transport rate and z_p value was determined for each geophone for SGC 1 and 2 and plotted in Figure 8. Wyss (2016) proposed a linear relationship of $z_p = 0.0064 \cdot q_s$ with $R^2 = 0.94$ to describe the relation between specific gravimetric bedload transport rates and corresponding z_p values at the bedload measurement station in the Erlenbach River (black line in Figure 8). As an alternative and more suitable to represent the physical process of signal saturation, an exponential function is fitted to Wyss's data (dotted black line in Figure 8). For bedload transport rates below 65 kg/(s·m) corresponding to $z_p \approx 0.4$, the difference between both fits is less than 13%, but increases rapidly beyond this limit. The best fit for the data set of (Müller-Hagmann, 2017), SGC1 and SGC 2 with a geophone inclination of 10° results in $z_p = 1 - \exp(-0.00456 \cdot q_s)$ with $R^2 = 0.75$ (light blue dotted line). Wyss (2016) stated that the effect of signal saturation at $z_p < 0.01$ is insignificant and can be neglected. However, in SBTs, high bedload transport rates with correspondingly high z_p values are possible and hence a certain degree of signal saturation can occur. Therefore, such effect of z_p is accounted for in the determination of the geophone calibration coefficient in the following.

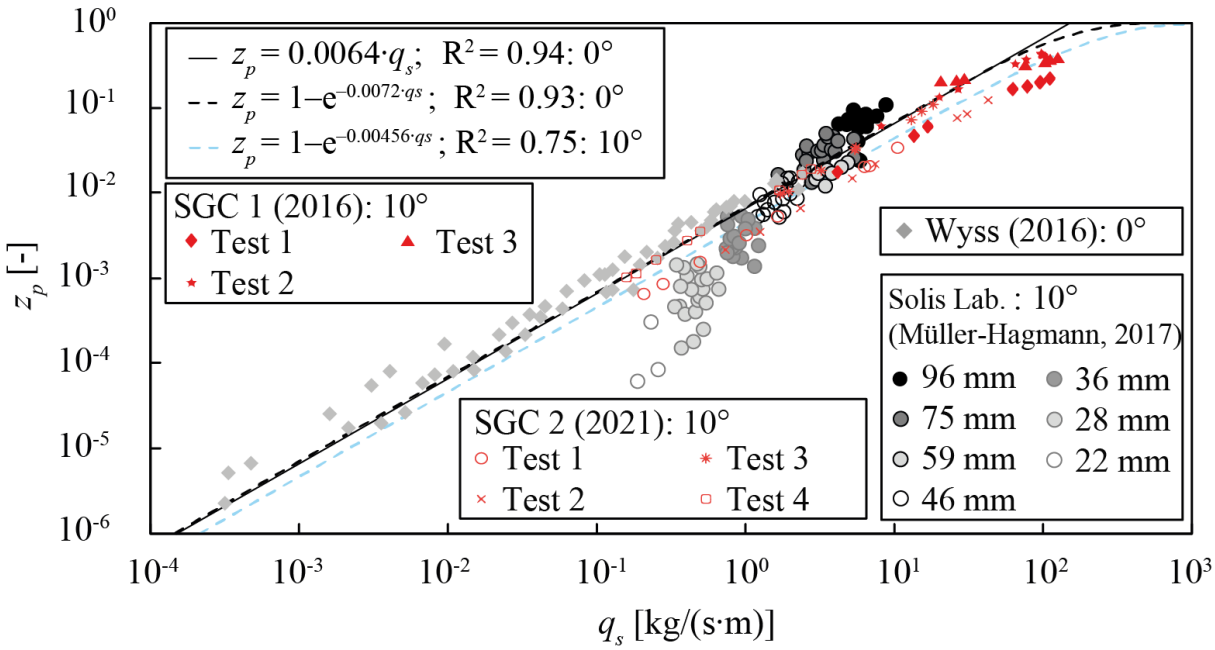

Figure 8: z_p vs sediment transport rate q_s at the Erlenbach River (Wyss, 2016) with the corresponding fit, as well as for the Müller-Hagmann (2017), SGC1 and SGC 2 data sets.

Figure 9 shows the calibration coefficients K_b, obtained from the Solis laboratory tests (Müller-Hagmann, 2017), SGC 1, SGC 2 (Table 4), laboratory tests of Morach (2011) and the Erlenbach tests of Rickenmann *et al.* (2013) as a function of flow velocities. Rickenmann *et al.* (2013) data show a decreasing trend of K_b with increasing flow velocity. This is due to increasing particle hop lengths causing fewer particle impacts on the geophone plate. A best fit is given by $K_b = 39.6 \cdot U^{-1.41}$ with $R^2 = 0.58$ for the Rickenmann data. $K_b = 1.34$ 1/kg was obtained by applying this equation to the mean flow velocity in the Solis SBT with $U \sim 11$ m/s (Figure 9). However, this value is questionable due to the unknown GSD (grain size distribution) of the bedload transport in the SBT and differences between this study and Rickenmann's study in terms of geophone inclination, particle properties and channel morphology (i.e., bed slope and roughness). On the contrary to Rickenmann's data, the data for the 10° inclined geophone plates were quasi-constant with a scatter because of the effect of particle diameter and z_p. This indicates that the calibration of a 10° inclined SPGS does not depend on the flow velocity for the investigated flow velocity range of $U = 3$ - 10 m/s. Hence, extrapolation of the laboratory results (Müller-Hagmann, 2017) at $U = 3$ m/s to calibrate the Solis SPGS for $U \approx 11$ m/s

would result in a significant underestimation of K_b and hence overestimation of bedload transport rates in the Solis SBT.

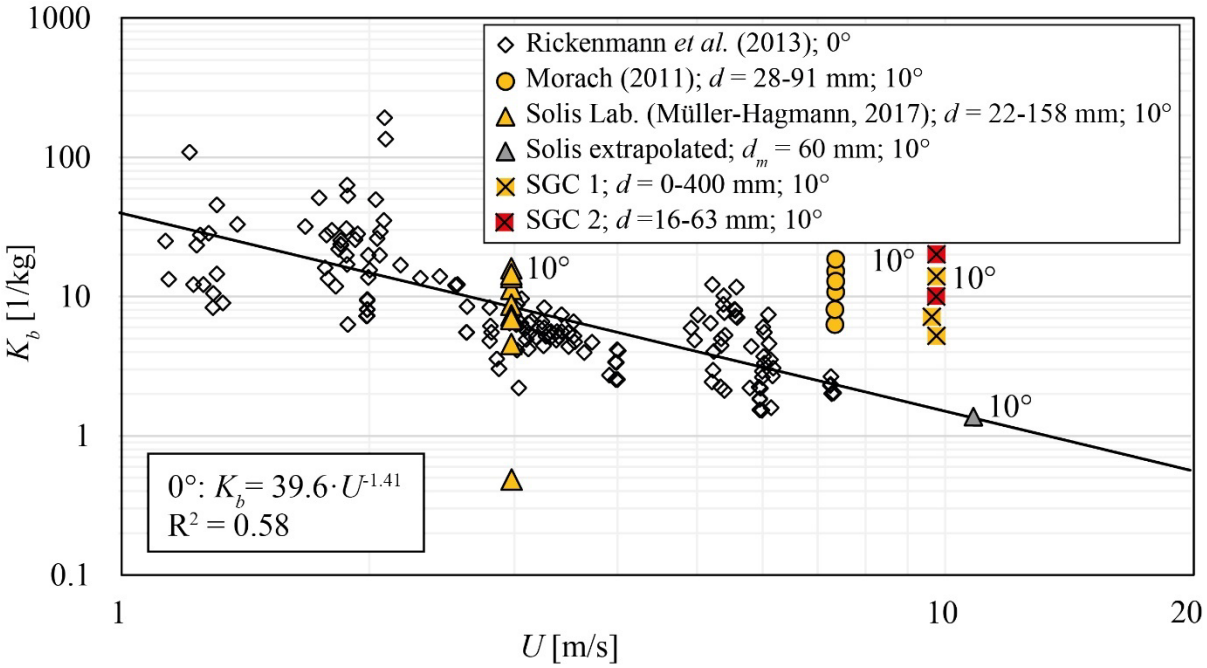

Figure 9: K_b as a function of flow velocity for different geophone inclinations and grain sizes including various data sets.

As shown in Figure 8, the sediment transport rate has a significant effect on z_p. Increasing the sediment transport rate causes more overlapping of particle impacts on a geophone (higher z_p values) and hence lower K_b values. In addition to the sediment transport rate, the sediment diameter also affects K_b (Tables 4 & 8, Müller-Hagmann, 2017). Figure 10 shows the relationship between z_p and K_b for each particle diameter for both SGC 1 and 2. K_b values of SGC 1 and 2 are listed in Table 8. Figure 10 shows that increasing z_p decreases K_b. For both size classes of 16-32 mm with d_m = 25 mm and 32-63 mm with d_m = 45 mm, there are three data points (2 points from SGC 2 and 1 point from SGC 1), and a power law function fits well the relation between z_p and K_b. The general form of K_b-z_p based on the fittings in Figure 10 is:

$$K_b = a \cdot {z_p}^b \qquad (15)$$

The power of b = −0.15 fits to the data. The particle size modifies the constant of the equation, a, listed in Table 9. For the size class of 0-400 mm with d_m = 210 mm, there is only one data from SGC 1 (2016), therefore the same power of b = −0.15 is assumed for this size class and the resulting 'a' value is 4.3 ($K_b = 4.3 z_p^{-0.15}$). By applying this equation, a K_b value of 6.6 was estimated for SGC 2 for z_p = 0.054, i.e., an averaged value of four tests (Table 4) (pink diamond in Figure 10). This estimated value is important to develop a relationship between d_m and K_b for SGC 2.

Table 8: Grain sizes and calibration coefficients of the three particle size classes obtained from the field calibrations. SGC 1: Solis Geophone calibration, field (2016). SGC 2: Solis geophone calibration, field (2021).

Test	16-32 mm	32-63 mm	0-400 mm
d_m [mm]	25	45	210
$K_{b,\ \mathrm{SGC\ 1}}$	6.80	13.55	5.05
$K_{b,\ \mathrm{SGC\ 2}}$	10.63 (q_s =14 kg/(sm))	18.68 (q_s = 58.2 kg/(sm))	-
$K_{b,\ \mathrm{SGC\ 2}}$	9.44 (q_s = 53.5 kg/(sm))	21.81 (q_s = 8.8kg/(sm))	-

Table 9: K_b - z_p fit coefficients for the field calibration tests

Tests (SGC 1 and 2)	16-32 mm	32-63 mm	0-400 mm
d_m [mm]	25	45	210
a	6.0	11.9	4.3
b	−0.15	−0.15	−0.15
R^2	0.70	0.91	0.88

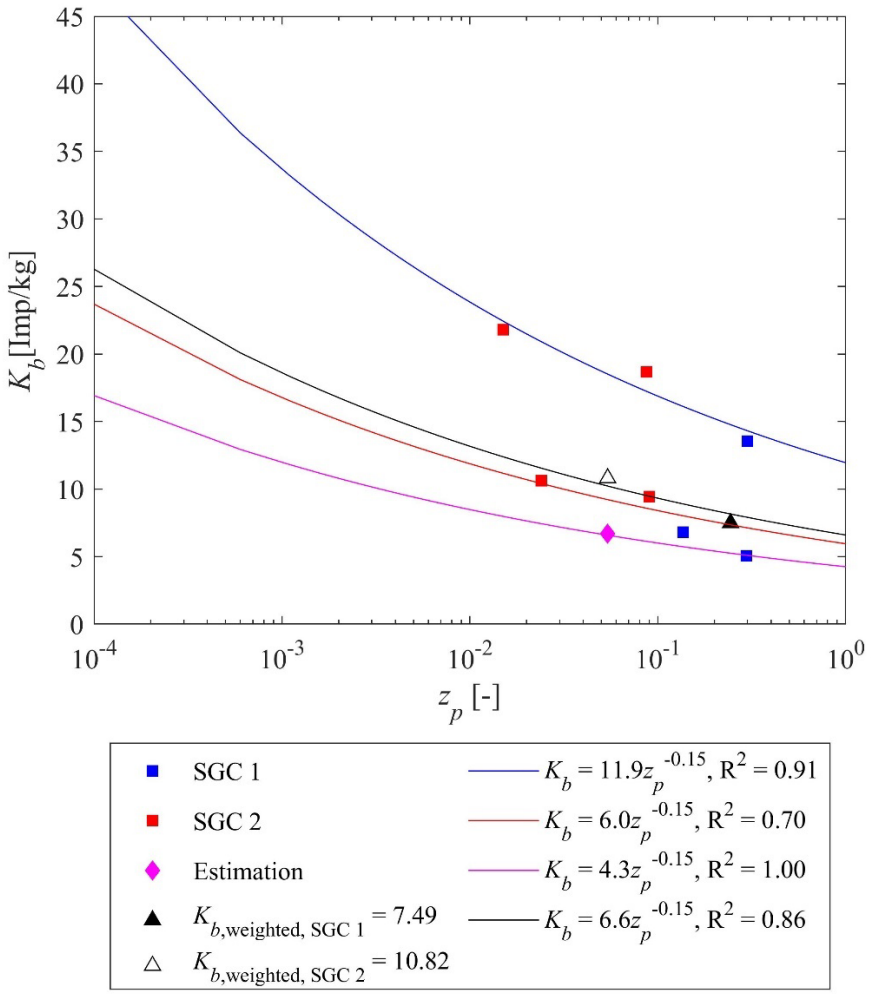

Figure 10: Calibration coefficient (K_b) as a function of impact overlap indicator (z_p) with the best fits to the different size groups. (___ red line is for d_m = 25 mm; ___ blue line is for d_m = 45 mm; ___ magenta line is for d_m = 210 mm; ___ black line is for weighted averaged K_b versus z_p). SGCF 1: Solis geophone calibration, field (2016); SGCF 2: Solis geophone calibration, field (2021).

Figure 11 shows the averaged calibration coefficient (K_b) as a function of mean particle size, d_m, for the SGC 1 and SGC 2 and corresponding Frechet fits as well as laboratory data from Morach (2011) and Müller-Hagmann (2017). The K_b value of d_m = 210 mm was estimated from the fit (pink diamond in Figure 10) because no calibration with the size class of 0-400 mm was conducted in SGC 2. The

difference between Morach's (2011) and other studies results from electric interference. This caused a significantly higher background noise, amplified the signal, and biased the results, in particular for small particles with low signal amplitudes in the range of the detection threshold. Although the data of SGC 1 and Solis laboratory data (Müller-Hagmann, 2017) are similar, the SGC 2 data are higher than those two data sets because of the effect of sediment transport rates on K_b. Both SGC 1 and 2 data are fitted to a Frechet equation. The general form of Frechet is as follows:

$$K_b = c_1 \cdot c_2 \cdot c_3 \cdot {c_4}^{c_3} \cdot \left[1 - exp\left(-\left(\frac{c_4}{D}\right)^{c_3}\right)\right]^{(c_2-1)} \cdot D^{-(c_3-1)} \cdot exp\left(-\left(\frac{c_4}{D}\right)^{c_3}\right) \quad (16)$$

The coefficients of the Frechet fit for SGC 1 and SGC2 are listed in Table 10. Due to different z_p values (transport rates) between SGC 1 and 2, two different fits are obtained, indicating that a functional relation between K_b and z_p is necessary for accurate bedload estimation. The weighted averaged K_b values of SGC 1 and 2 based on the particle size distribution of Solis (Figure 4) are calculated from both Frechet fits. The weighted averaged K_b values and corresponding weighted averaged z_p values are plotted and fitted in Figure 10. The weighted averaged K_b-z_p equation from the fit is:

$$K_b = 6.6 \cdot {z_p}^{-0.15} \quad (17)$$

Applying this equation, the K_b value and hence sediment transport mass are determined for each geophone using the corresponding z_p value determined from the signals recorded at each SBT operation between 2017 and 2020. The results are listed in Table 11.

Table 10: Frechet fit (Figure 11, Eq. 16) coefficients for the field calibration tests.

Test	c_1	c_2	c_3	c_4	R^2
SGC 1	15000	0.044	1.850	48.0	0.97
SGC 2	16090	0.083	1.497	55.6	1.00

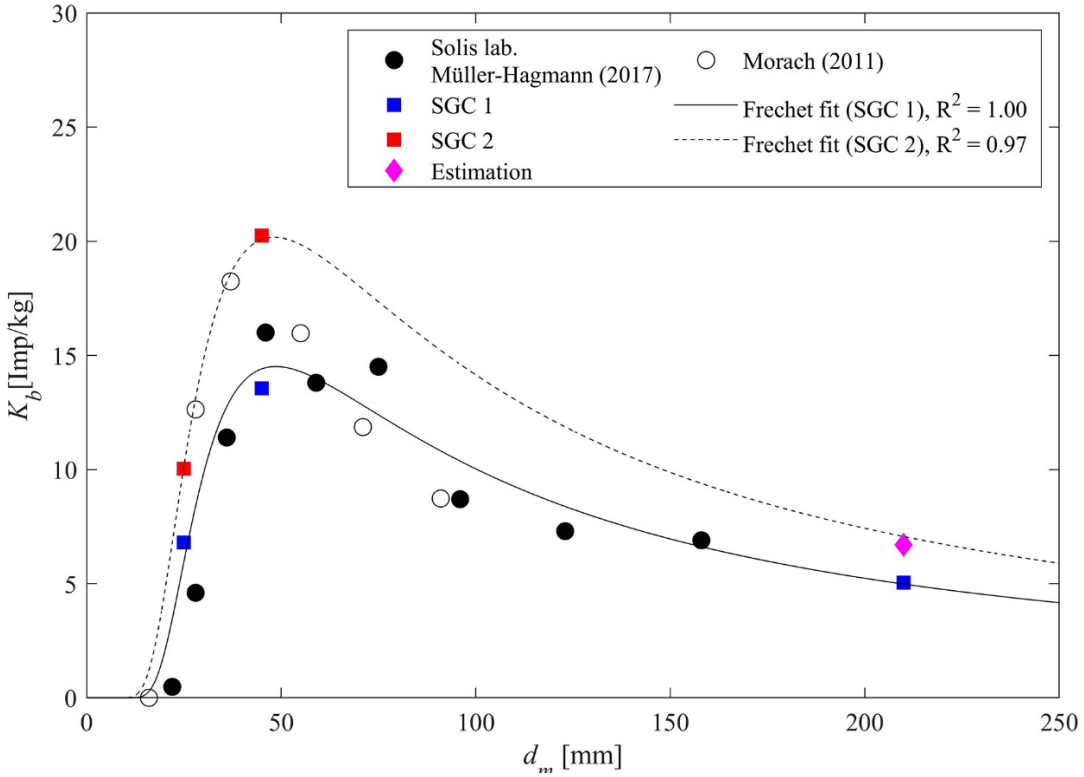

Figure 11: Calibration coefficient (K_b) versus mean grain size (d_m) with the Frechet fits for the field calibration tests. SGC 1: Solis geophone calibration (2016); SGC 2: Solis geophone calibration (2021).

Table 11: Total bedload estimation for Solis SBT operations between 2017-2020.

Geophone / Event (yr)		1	2	3	4	5	6	7	8	Total [to]
1 (06/2017)	z_p	0.022	0.035	0.046	0.050	0.043	0.017	0.017	0.005	
	K_b (Eq. 17)	11.9	11.1	10.6	10.5	10.7	12.3	12.4	15.0	
	Mass [to]	64	107	162	166	145	47	48	9	748
2 (06/2018)	z_p	0.012	0.017	0.015	0.009	0.005	0.002	0.001	0.001	
	K_b (Eq. 17)	13.0	12.4	12.5	13.6	14.9	16.9	18.6	19.4	
	Mass [to]	55	82	79	38	19	7	3	2	285
3 (09/2018)	z_p	0.009	0.013	0.019	0.024	0.025	0.017	0.017	0.012	
	K_b (Eq. 17)	13.5	12.8	12.2	11.7	11.6	12.3	12.3	13.0	
	Mass [to]	49	75	116	146	155	98	102	61	802
4 (10/2018)	z_p	0.008	0.011	0.011	0.016	0.018	0.015	0.013	0.012	
	K_b (Eq. 17)	13.9	13.3	13.1	12.5	12.3	12.6	12.8	13.1	
	Mass [to]	19	27	32	46	51	38	37	30	280

5 (06/2019)	z_p	0.050	0.069	0.090	0.085	0.072	0.040	0.020	0.005	
	K_b (Eq. 17)	10.5	10.0	9.6	9.7	10.0	10.8	12.1	14.7	
	Mass [to]	975	1'408	2'006	1'741	1'461	749	339	63	8'742
6 (06/2019)	z_p	0.112	0.145	0.151	0.146	0.099	0.042	0.019	0.006	
	K_b (Eq. 17)	9.3	8.9	8.9	8.9	9.5	10.8	12.1	14.3	
	Mass [to]	7'676	10'680	11'874	9'796	6'879	2'570	926	215	50'616
7 (08/2019)	z_p	0.009	0.005	0.002	0.001	0.000	0.000	0.000	0.000	
	K_b (Eq. 17)	13.6	14.6	16.9	20.0	24.7	29.8	34.6	39.7	
	Mass [to]	8	4	2	0	0	0	0	0	14
8 (08/2020)	z_p	0.067	0.091	0.075	0.038	0.021	0.011	0.003	0.002	
	K_b (Eq. 17)	10.1	9.6	9.9	11.0	11.9	13.1	15.7	16.7	
	Mass [to]	1'723	2'299	1'963	776	412	175	53	29	7'423
									total	**68'910**

3.1.2 Hydraulic operating conditions

Figure 12 shows the time series of the inflow into the Solis reservoir, the discharge through the Solis SBT and the water level of the Solis reservoir for the years 2017 to 2020. Pink vertical lines correspond to the dates of 3D laser scanning of the test fields. During the period between 2017 and 2020, a one-year flood (HQ_1) occurred in late May 2018, a five-year flood (HQ_5) took place in June 2019, with a maximum hourly inflow of 183 m³/s (170 m³/s daily mean) into the Solis reservoir and again a one-year flood (HQ_1) occurred at the end of August 2020. The Solis SBT discharged an hourly maximum of 150 m³/s (135 m³/s daily mean) during the HQ_5 event, while the design (index d) discharge is $Q_{SBT,d}$ = 170 m³/s. Between 2017 and 2020, the SBT was in operation for a total of 227 h. During and after the HQ_5 flood, the SBT was in operation non-stop between 03rd June 2019 and 05th July 2019, i.e., over 33 days.

In total, the SBT was in operation 14 times between 2017 and 2020, four times of which the reservoir water level was lowered below the drawdown level of 816 m asl. Most importantly, during the HQ_5 flood in June the reservoir level was as low as 813 m asl (Figure 12c). It was shown by Müller-Hagmann (2017, Fig. 6.14) that significant bedload transport to the SBT intake occurs for reservoir levels of 815 m asl or lower, as the shear stress at the pivot point of the delta of aggregated sediment is too low for higher water levels to initiate bedload transport.

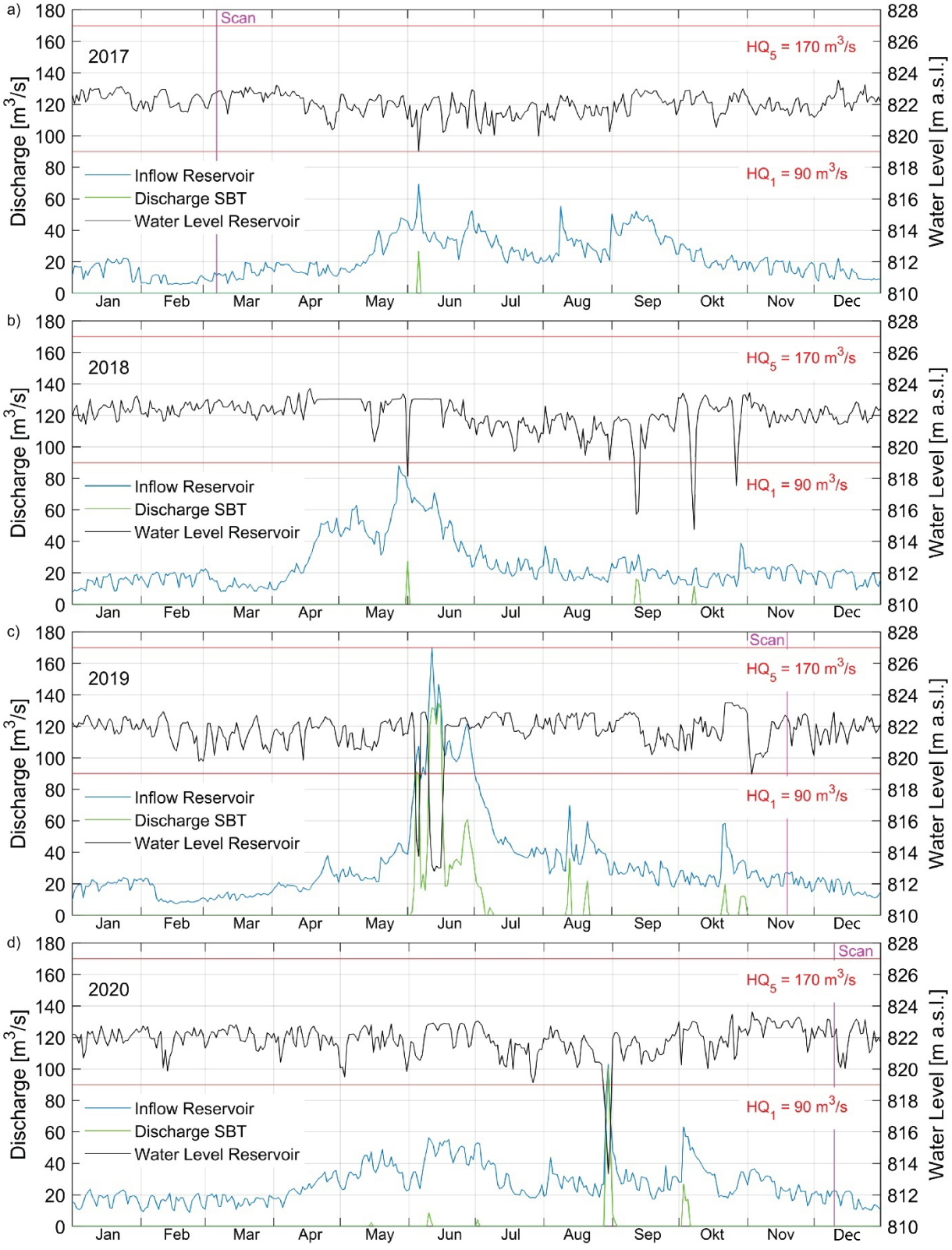

Figure 12: Time series of inflow at reservoir, discharge at SBT and water level at reservoir in Solis between 2017 and 2020 (daily resolution). Additionally, the HQ1 and HQ5 flood discharges as well as the laser scan measuring campaigns are indicated.

3.1.3 Sediment transport

The instantaneous bedload transport rates were measured using a Swiss Plate Geophone System (SPGS) with eight geophone plates located at the outlet of the SBT. During 2017 and 2020, a total bedload mass (solid volume) of about 68'910 to (26'004 m^3) bypassed the reservoir through the SBT (Table 11). Considering the operation hours of about 227 h between 2017 and 2020 (see section 3.1.2), a mean bedload transport rate of 84.32 kg/s (0.032 m^3/s) is determined. The sediment density thereby assumed is 2.65 to/m^3.

Regarding only the HQ_5 flood event in 2019, the SBT was continuously operation at different reservoir water levels. During the operation, a total bedload mass (volume) of about 8'742 to (~3'300 m^3) and about 50'616 to (19'100 m^3) passed through the SBT at about 815 m and 813 m a.s.l., respectively (Figure 13). These correspond to an average bedload transport rates of 72.23 kg/s (0.027 m^3/s) and 126 kg/s (0.048 m^3/s), respectively. Figure 13 shows that the bedload sediments passed the SBT only while the reservoir level was lowered to about 816 m a.s.l. and below. When the water level was around 822 m a.s.l., no sediments passed through the SBT, although the flood event still lasted for several days with a reservoir inflow of 100 to 120 m^3/s (higher than HQ_1) and with a SBT discharge between 20 and 60 m^3/s. This result evidently shows that the bypass efficiency of the SBT is strongly affected by the reservoir operation.

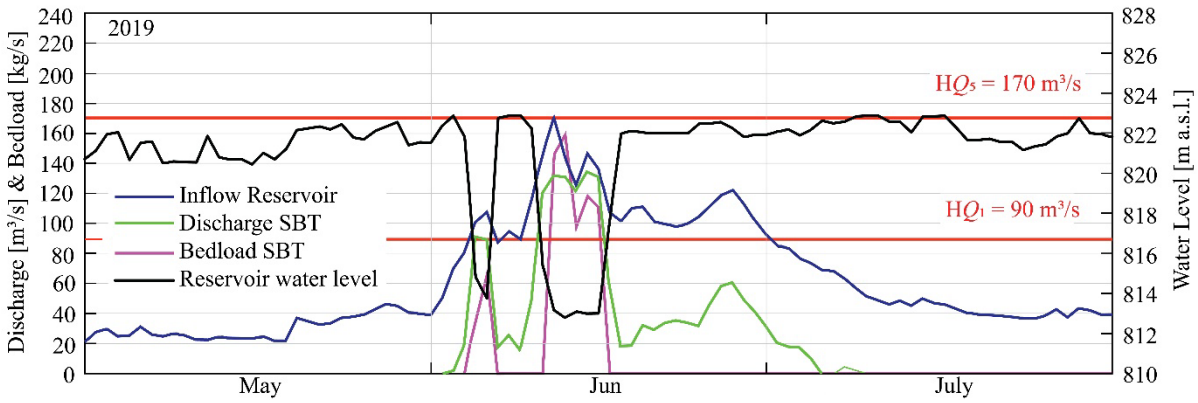

Figure 13: Time series of inflow to reservoir, discharge through SBT, bedload through SBT and reservoir water level in Solis between May and August 2019 (daily resolution). Additionally, the HQ_1 and HQ_5 flood discharges are indicated.

3.1.4 Hydroabrasion

Based on visual inspections by the operator, only the flood in June 2019 caused measurable abrasion on the SBT invert (F0 and F7) as well as the six implemented test fields F1 to F6. However, the measuring campaigns of 07th March 2017 and 10th December 2020 were taken into account to quantify the total abrasion depths during the study period (Figure 14 to Figure 21). At the up- and downstream borders of the test fields, the influence of the laser scanner shadow and the effects of the steel beam transition between the different test fields are visible. Therefore, a stripe of 2 m length upstream and downstream of each test field was removed from the calculations of the mean and maximum abrasion depths. The largest spatially averaged abrasion depth of 36 mm was determined at the test field F7 (NC, (standard lining)), while the lowest value of 1 mm was determined at the test field F5 (CB, cast basalt plates) (Table 12). Steel armouring plate (SA, F6) performs better than the tested concretes. The maximum longitudinally averaged abrasion depth of 49.90 mm (locally 86 mm, Table 12) was measured at the test field F7 (NC, normal concrete, i.e., standard lining of the SBT) (Figure 22). The best performing concrete is HAC (Potassium aluminate cement concrete, F3) while UHPC (Ultra high-performance concrete, F4) shows the worst performance (Table 12). The transversal cross-sections of the test fields, averaged over the effective field length of 6 m, show that the abrasion has a rather symmetric pattern with higher abrasion at the tunnel centre and two incision channels about 25% of the tunnel width away from the sidewalls (Figure 22). This was expected

because of the low tunnel width to water depth aspect ratios < 2 during the 2019 flood (4.4 m of tunnel width / 2.6 m water depth = 1.7). At such low aspect ratios, strong secondary currents occur in the tunnel and hence bed shear stresses are higher in the tunnel centre than close to the tunnel sidewalls (Demiral *et al*., 2020). Furthermore, such a pattern indicates that the effect of upstream tunnel bend on the flow field and sediment transport diminishes on the test fields, which is far away from the first bend. In longitudinal direction, a wavy abrasion pattern is observed, which is attributed to the hop length of saltating bedload particles (Figure 23). Figure 24 to Figure 31 give a visual impression of the condition of the test fields.

Table 12: Mean hydroabrasion of test fields F0 to F7 between 2017 and 2020 at Solis SBT for x = [2,8] m at each test field.

Test field	Abrasion [mm]			
	2017 - 2020			
	Mean	Max local	Max longitudinally averaged (Figure 22)	Standard dev.
F0 (NC)	29	48	36.4	9
F1 (HSC)	29	57	36.4	10
F2 (LSC)	35	61	42.4	12
F3 (HAC)	10	29	13.6	3
F4 (UHPC)	29	57	37.6	11
F5 (CB)	2	7	1.9	1
F6 (SA)	3	7	3.4	1
F7 (NC)	36	86	49.9	12

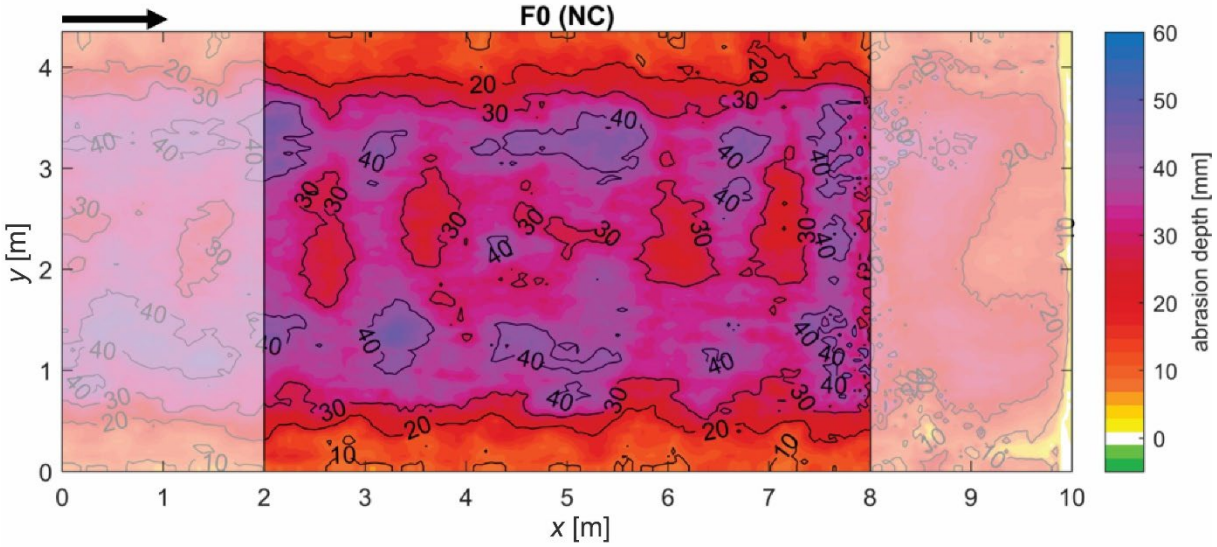

Figure 14: Abrasion topography of test field F0 (Normal concrete, NC (standard lining)) between 2017 and 2020 in Solis SBT with mean abrasion depth of 29 mm.

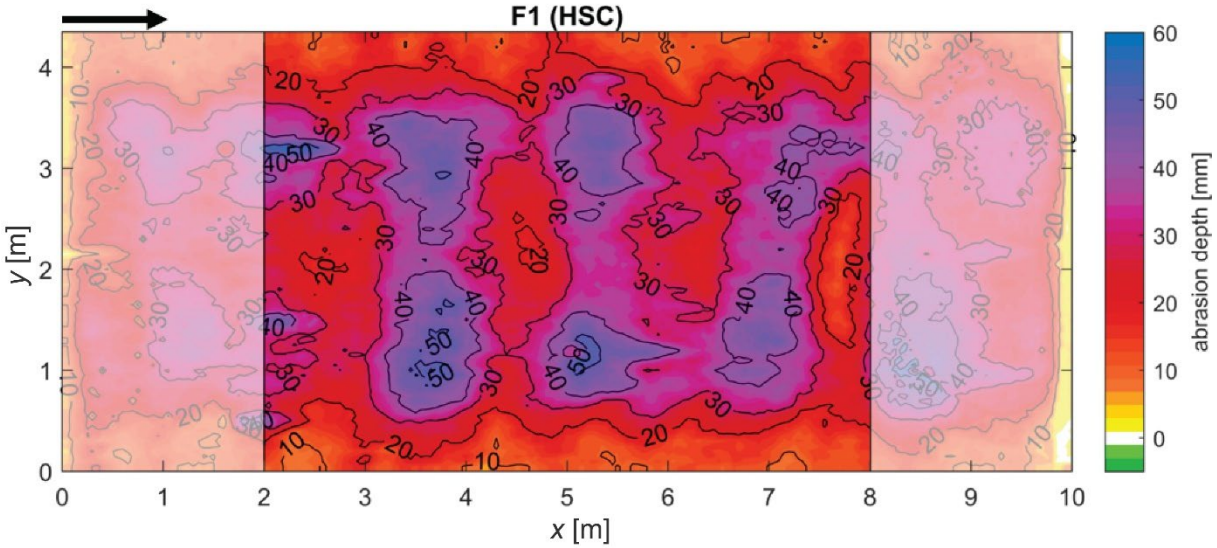

Figure 15: Abrasion topography of test field F1 (High performance concrete with steel fibers, HSC) between 2017 and 2020 in Solis SBT with mean abrasion depth of 29 mm.

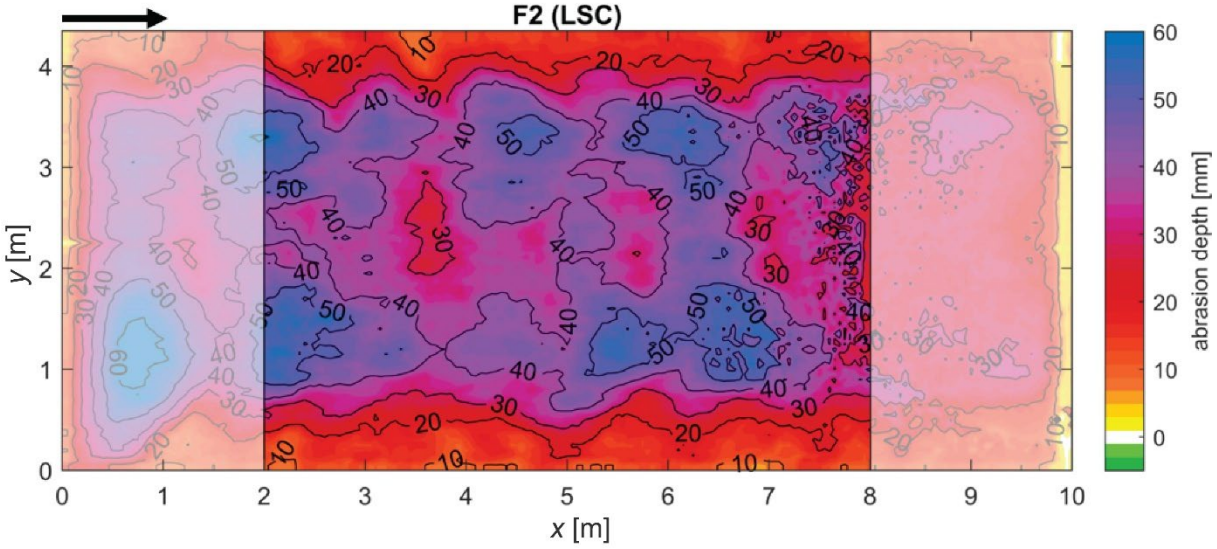

Figure 16: Abrasion topography of test field F2 (Low-shrinkage with high modulus polymer fibers, LSC) between 2017 and 2020 in Solis SBT with mean abrasion depth of 35 mm.

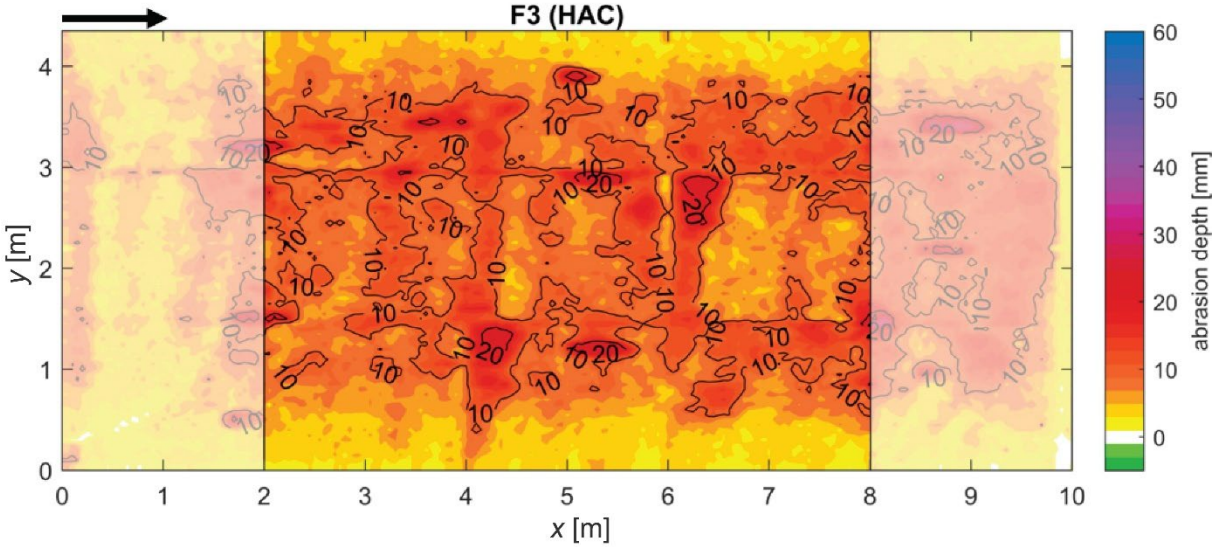

Figure 17: Abrasion topography of test field F3 (Potassium aluminate cement concrete, HAC) between 2017 and 2020 in Solis SBT with mean abrasion depth of 9 mm.

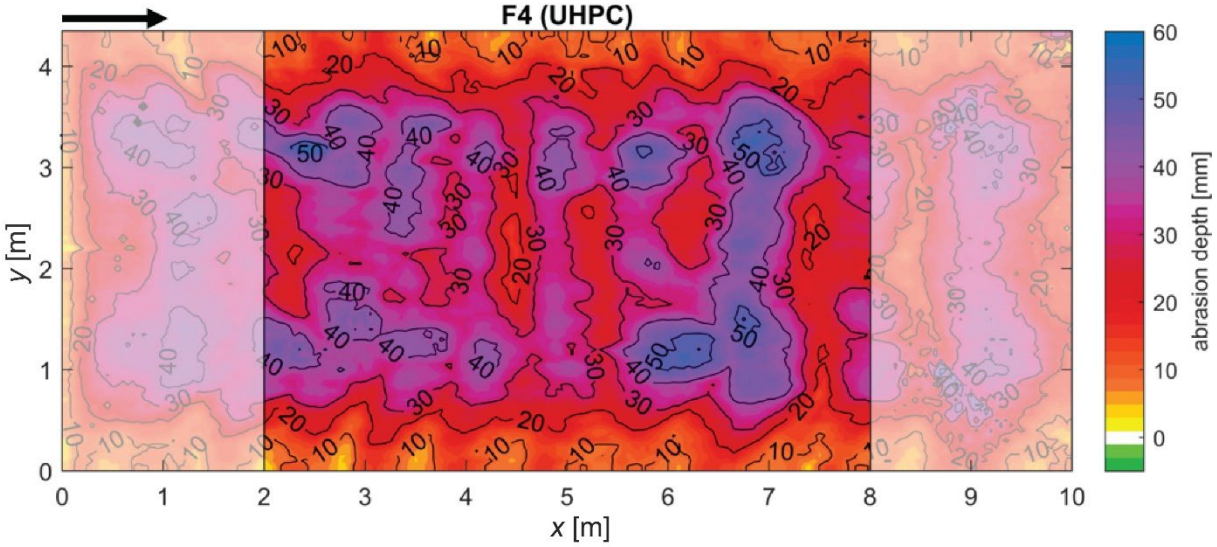

Figure 18: Abrasion topography of test field F4 (Ultra high-performance fiber concrete, UHPC) between 2017 and 2020 in Solis SBT with mean abrasion depth of 29 mm.

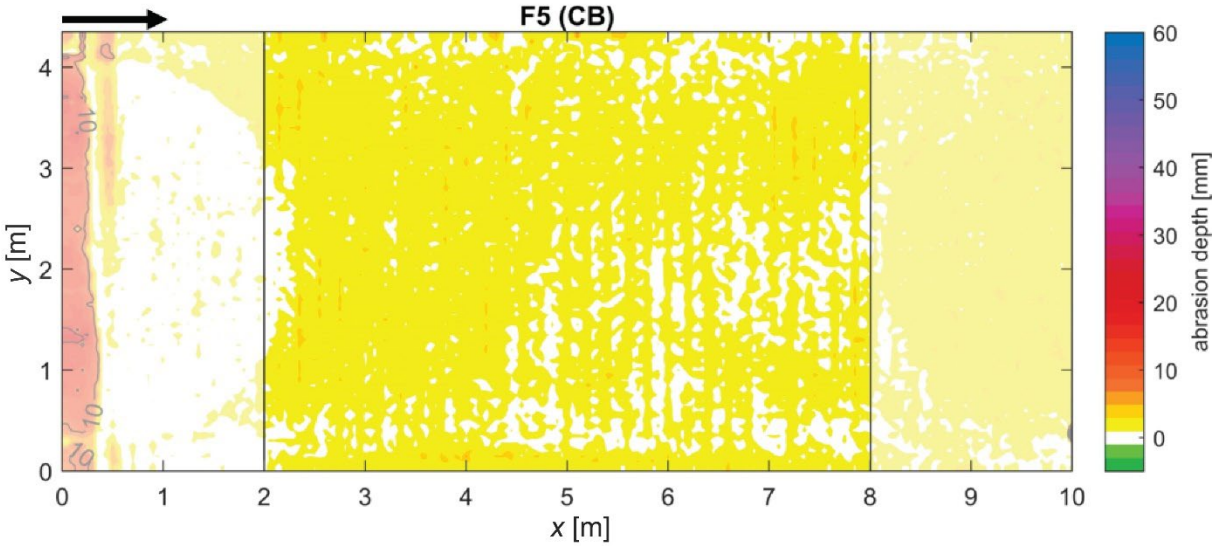

Figure 19: Abrasion topography of test field F5 (Cast basalt plates, CB) between 2017 and 2020 in Solis SBT with mean abrasion depth of 1 mm.

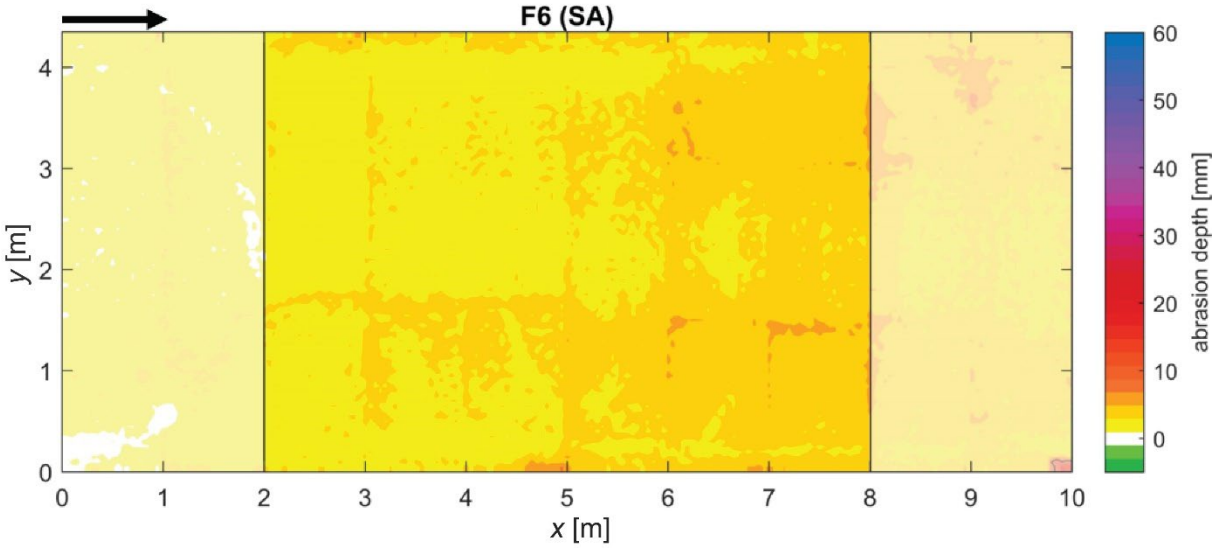

Figure 20: Abrasion topography of test field F6 (Steel armoring plate, SA) between 2017 and 2020 in Solis SBT with mean abrasion depth of 3 mm.

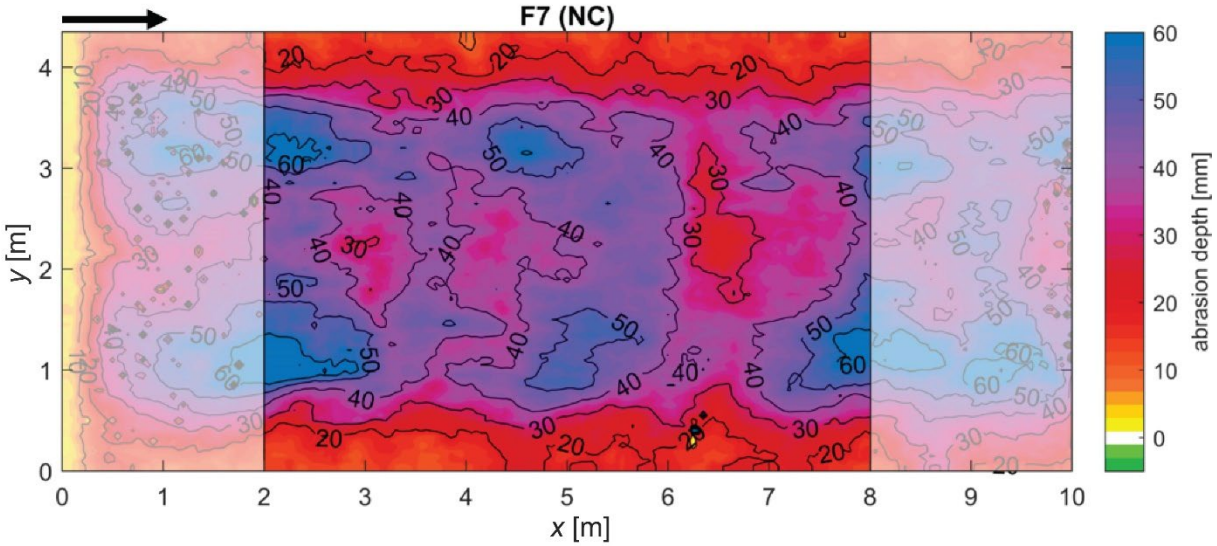

Figure 21: Abrasion topography of test field F7 (Normal concrete, NC (standard lining)) between 2017 and 2020 in Solis SBT with mean abrasion depth of 36 mm.

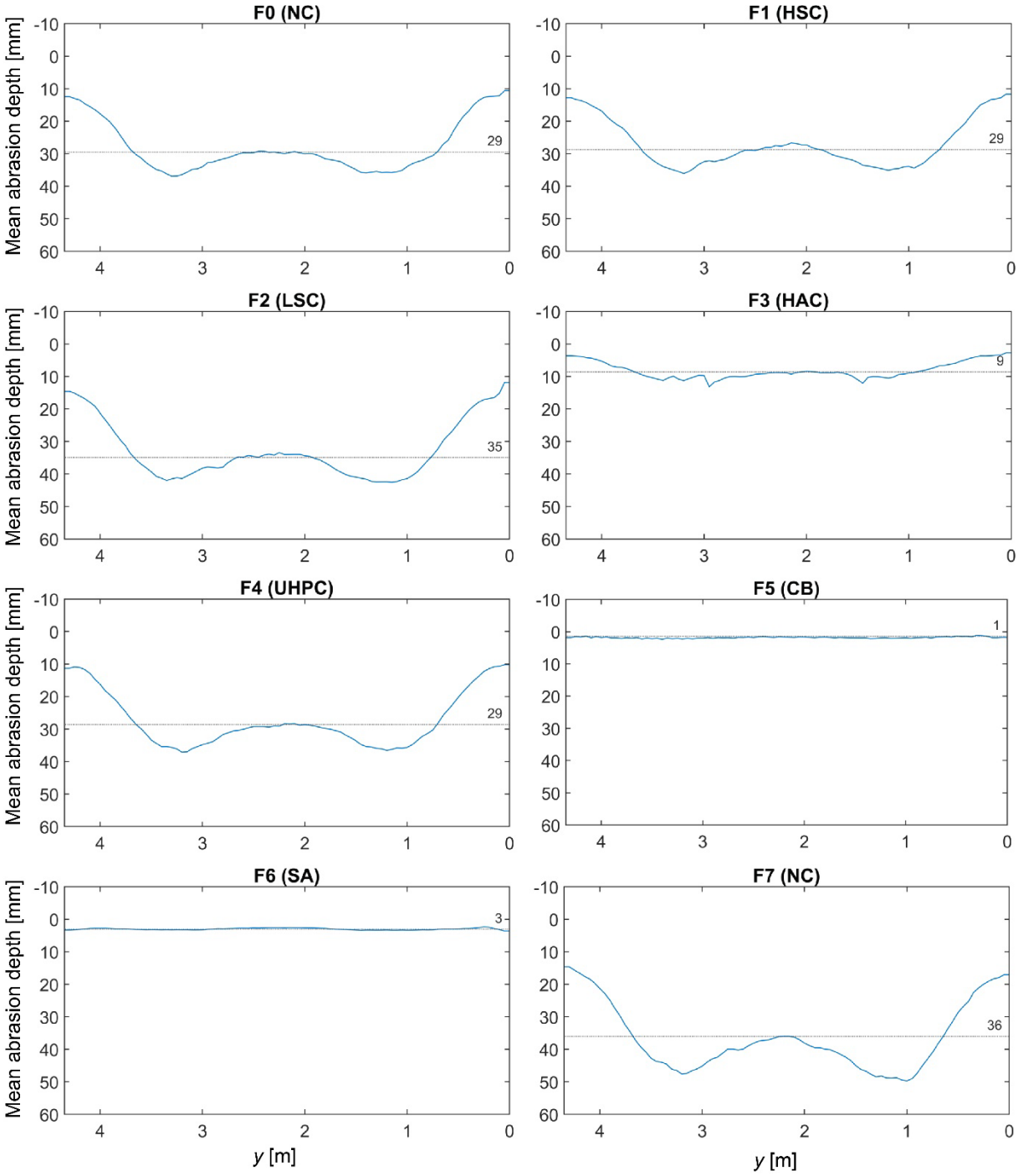

Figure 22: Longitudinally averaged transversal abrasion profiles of test fields F0 to F7 between 2017 and 2020 in Solis SBT (view in flow direction). The dotted line represents the mean abrasion depth of the test field each.

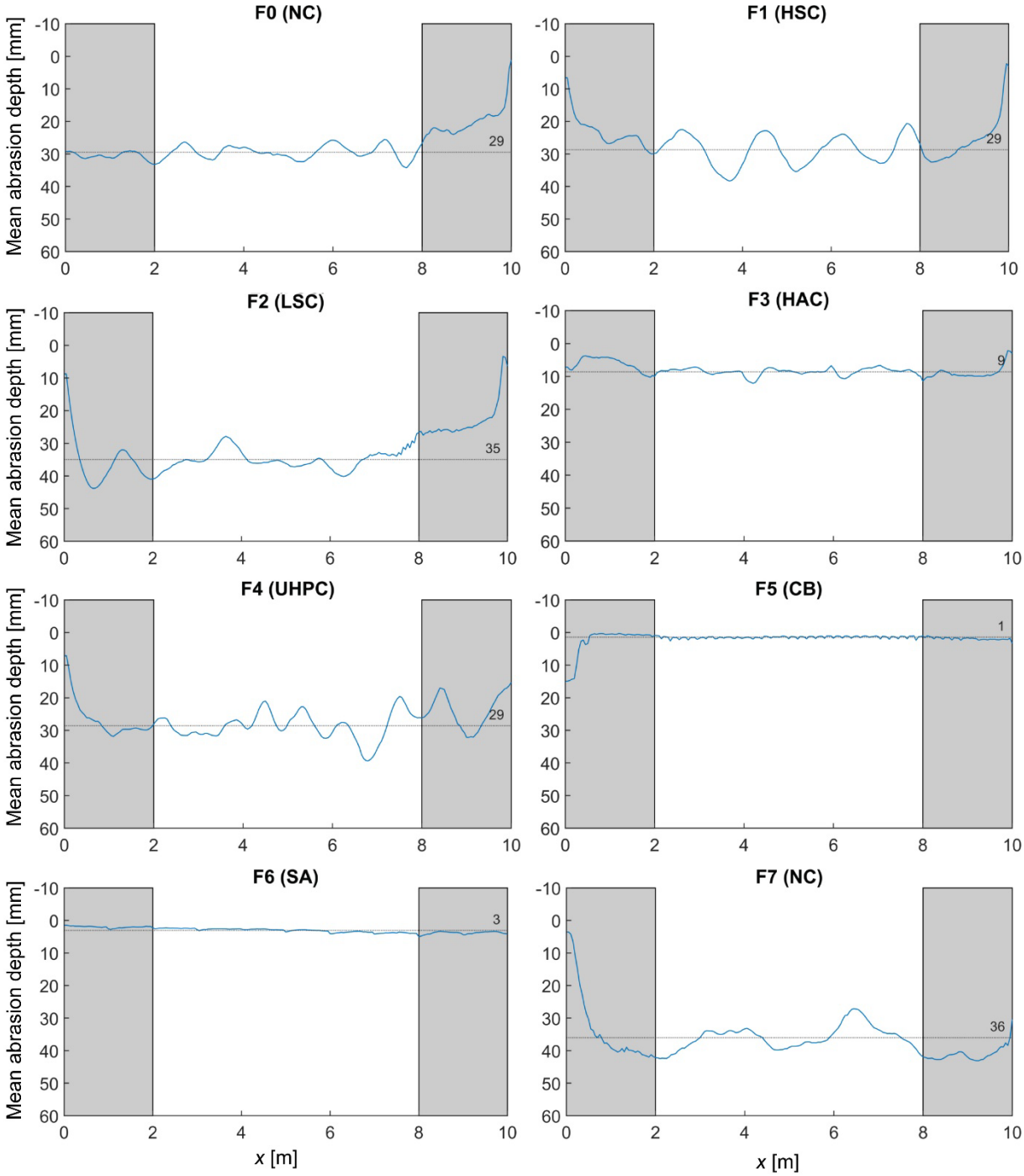

Figure 23: Transversally averaged longitudinal abrasion profiles of test fields F0 to F7 between 2017 and 2020 in Solis SBT (flow direction from left to right). The dotted line represents the mean abrasion depth of the test field each. The effective test field length is indicated by the white area.

Figure 24: Picture of test field F0 (NC) during measuring campaign of 10th December 2020 at Solis SBT, view in flow direction.

Figure 25: Picture of test field F1 (HSC) during measuring campaign of 10th December 2020 at Solis SBT, view in flow direction.

Figure 26: Picture of test field F2 (LSC) during measuring campaign of 10th December 2020 at Solis SBT, view in flow direction.

Figure 27: Picture of test field F3 (HAC) during measuring campaign of 10th December 2020 at Solis SBT, view in flow direction.

Figure 28: Picture of test field F4 (UHPC) during measuring campaign of 10th December 2020 at Solis SBT, view in flow direction.

Figure 29: Picture of test field F5 (CB) during measuring campaign of 10th December 2020 at Solis SBT, view in flow direction.

Figure 30: Picture of test field F6 (SA) during measuring campaign of 10th December 2020 at Solis SBT, view in flow direction.

Figure 31: Picture of test field F7 (NC) during measuring campaign of 10th December 2020 at Solis SBT, view in flow direction.

3.1.5 Sediment properties

The abrasiveness of the sediments, sampled from the Albula in summer 2019, was determined by analyzing the particle shape and hardness. The results show that the particle shapes of the samples are rounded to sub-rounded according to ISO (2013). The results of the XRD analysis are shown in Figure 32. The content of hard minerals, i.e., feldspar and quartz with a Mohs hardness of 6 and 7, respectively, is roughly 20%, while soft minerals with a Mohs hardness of less or equal to 3.5 amount to roughly 80%. The bulk hardness varies between 3.5 and 3.7 and no clear trend is observed between the particle size and the mineral composition of the particles. Overall, the results indicate a low abrasiveness of the Solis catchment sediment, explaining why cast basalt plates with high Mohs hardness above 8.5 perform best against hydroabrasion compared to other test materials at Solis SBT.

The portion of each mineral slightly varies for the different particle size classes. Such variations might be attributed to uncertainties and errors of the applied method and analysis and/or physical processes occurring in the catchment and along the river reach. However, the standard deviation of the XRD results is less than 0.15%, which is an order of magnitude below the results' variation and hence is not at the origin of the variation in mineralogy with particle size. By assuming a spherical particle shape and a bulk density of 2'650 kg/m^3 as rough estimates, the minimum number of particles was 630, resulting in an error of less than ±3% at a confidence interval of 95%. Therefore, the results can be regarded as representative and the observed variations in bulk Mohs hardness of 4% cannot be attributed to such an uncertainty only. Such variations might also be explained by the different abrasion rates of sediment particles of different lithology producing different degrees of downstream fining (Kodama, 1994a, b). The sediment arriving at Solis originates from a large catchment area of 900 km^2 consisting of various smaller sub-basins with variations in lithology, transport distance, channel morphology and sediment supply rate. This may result in the observed variations of mineral composition and hardness. Overall, the observed variation is not judged decisive for the general observed SBT abrasion, neither in terms of abrasion depth nor in terms of pattern.

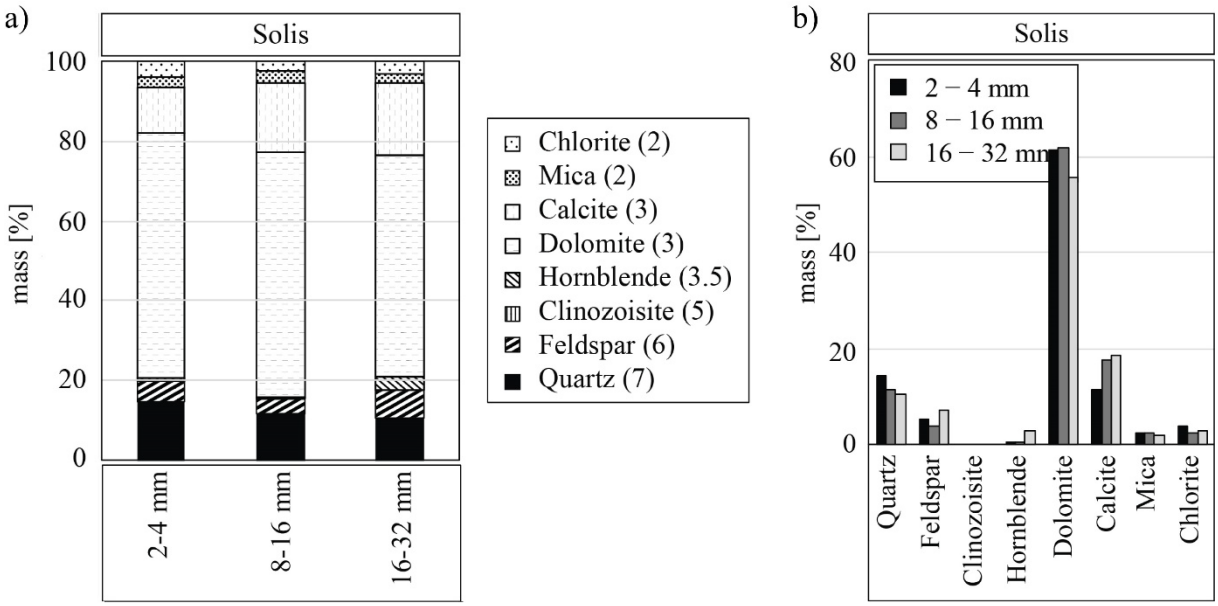

Figure 32: Mineralogical composition of the sediment transported through the Solis SBT arranged by a) sediment size and b) mineral type.

3.2 Pfaffensprung SBT

3.2.1 Hydraulic operating conditions

The Pfaffensprung reservoir is fed by the River Reuss and by the turbined water of the hydropower station Wassen. At the inlet of the reservoir, an intake structure diverts a maximum of 16 m^3/s from the Reuss into the reservoir. The excessive water is diverted into the SBT. At a discharge of more than 40 m^3/s in the Reuss, no water is diverted into the reservoir anymore. At the inlet to the reservoir, a guiding wall helps to divert the water into the SBT at high flows. At a discharge of more than 150 m^3/s in the Reuss, some water can overtop the guiding wall and enter the reservoir. The one-, ten- and 50-year flood discharges in the Reuss are 220 m^3/s, 360 m^3/s and 460 m^3/s, respectively (VAW, 1992).

The mean discharge through the Pfaffensprung SBT between 2012 and 2020 amounts to 10.4 m^3/s during its operation, varying between 3.8 and 19.4 m^3/s for single years. Considering only the discharge during bed load transportation, the mean discharge is 64 m^3/s (Table 13). The maximum discharge was measured on 03rd October 2020 with 248 m^3/s based on 15 minutes data (141 m^3/s daily mean), thus reaching the maximum discharge capacity of $Q_{SBT,max}$ = 240 m^3/s, while the design discharge is given with $Q_{SBT,d}$ = 220 m^3/s. For the period 2012 to 2020, the SBT was in operation during about 150 hours per year on average, varying between 22 and 420 hours for single years. All relevant data are listed in Table 13. Figure 33 shows the time series of of discharge (daily resolution) of the SBT. Pink vertical lines correspond to the dates of 3D laser scanning of the test fields. The last laser scan measuring campaign was conducted in January 2021 and hence not seen in Figure 33.

Table 13: Mean and maximum discharge as well as duration of operation between 2012 and 2019 at Pfaffensprung SBT. Maximum values are based on 15 minutes data.

Year	Mean SBT discharge during operation [m^3/s]	Mean SBT discharge during BL transport [m^3/s]	Max SBT discharge [m^3/s]	Duration of SBT operation [h]
2012	19.2	75	241	170
2013	15.4	57	245	296
2014	9.9	57	157	46
2015	7.6	40	119	154
2016	6.0	72	190	64
2017	3.8	55	98	22
2018	4.0	36	91	48
2019	19.4	67	242	420
2020	7.9	114	248	50
Average	10.4	64		149
Total				1270

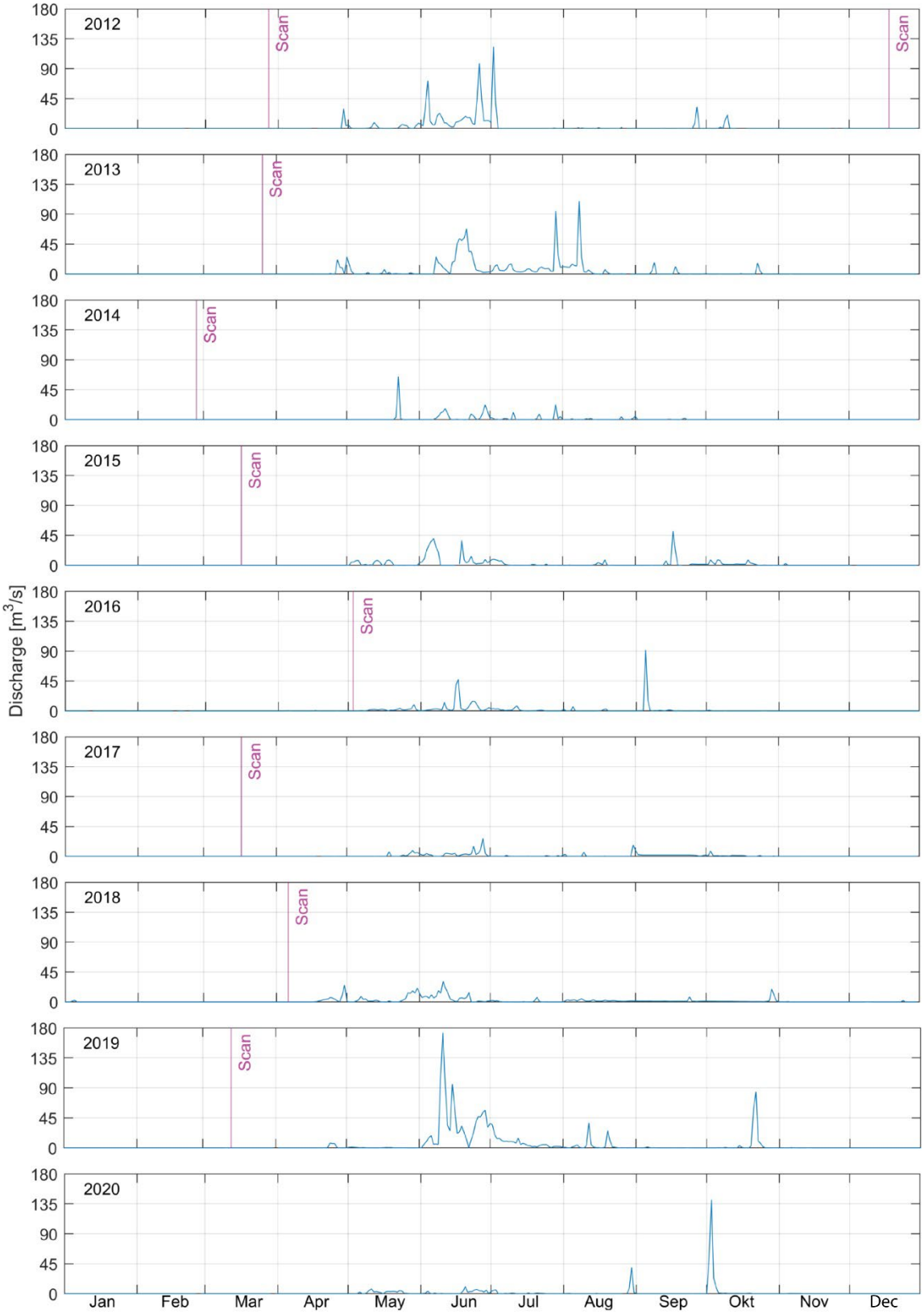

Figure 33: Time series of discharge (daily resolution) of the SBT Pfaffensprung for the years 2012 to 2020. Additionally, the laser scan measuring campaigns except the one in Jan 2021 are indicated as vertical lines.

3.2.2 Sediment transport

As there is no bedload transport measuring system at Pfaffensprung SBT, the bedload transport was estimated based on the effective bedload transport in the River Reuss. It is assumed that there is bedload transport in the Reuss as soon as the critical discharge Q_c = 38 m³/s is reached (Müller-Hagmann, 2017). The mean annual bedload mass and volume amount to 73'000 tons and 27'500 m³, respectively (Table 14). Considering the average operation hours of about 149 h when bedload transport occurred (see section 3.2.1), a mean bedload transport rate of 136 kg/s (0.051 m³/s) is calculated. The assumed sediment density is 2.65 to/m³.

Table 14: Estimated yearly bedload transport masses and volumes between 2012 and 2020 at Pfaffensprung SBT.

Year	2012	2013	2014	2015	2016	2017	2018	2019	2020	Mean
Bedload transport mass [10³ to/yr]	123	129	19	18	40	3	4	237	88	73
Bedload transport volume [10³ m³/yr]	46	49	7	7	15	1	1	90	33	28

3.2.3 Hydroabrasion

The first laser scan of the tunnel inverts was conducted on 28th March 2012. Table 15 and Figure 34 to Figure 37 show the hydroabrasion maps at the two test fields calculated by subtracting the first scan from the last scan conducted on 7th January 2021. During the first measuring campaign on 28th March 2012, the used laser scanner was not able to cover the whole test field area. Therefore, only an effective length of 6 meters of the whole test field length of 10 m could be used for the analysis. The spatially averaged and local maximum abrasion depths at the test field F1 (C, high strength concrete) are 61 mm and 124 mm, respectively, while they are 8 mm and 21 mm at the test field F2 (G, granite), respectively. This result clearly shows that the abrasion resistance of granite is more than 7.5 times higher than of the used concrete.

Along the SBT some water ingresses and flows on the floor towards the SBT outlet. This water is collected in front of the test fields and diverted on the left side using mobile pipes (Figure 38 and Figure 39). Therefore, in this area no measurements of the abrasion depth could be made (see gray areas in Figure 34 and Figure 35).

The abrasion is slightly more pronounced at the right tunnel side in flow direction (Figure 344 and 36). This asymmetry was caused by the secondary currents occurring due to the upstream tunnel bend. Such secondary currents transported most of the sediments towards the inner curve (right side) where the bed shear stress was higher and therefore caused a higher abrasion at the right side of the test field (Figure 34 and Figure 36). At the F2 test field (G, granite), higher abrasion depths are determined at the joints of the granite plates and no clearly pronounced abrasion at the right tunnel side is observed, as at the test field F1 (Figure 35 and Figure 36). This indicates that the effect of the secondary currents on the hydroabrasion pattern diminishes on the granite test field. This result may be related to: (i) more homogeneous characteristic of the granite compared to the concrete, (ii) a slight inclination i.e., 1.7% of the bottom from the left to the right side, and/or (iii) significantly less abrasion of the granite. Figure 38 and Figure 39 give a visual impression of the condition of the test fields.

Table 15: Mean abrasion depths of test fields F1 and F2 between 2012 and 2020 at Pfaffensprung SBT.

Test field	Abrasion [mm]			Test field	Abrasion [mm]		
	Mean	Max	Standard dev.		Mean	Max	Standard dev.
F1 (C)	61	124	29	F2 (G)	8	21	4

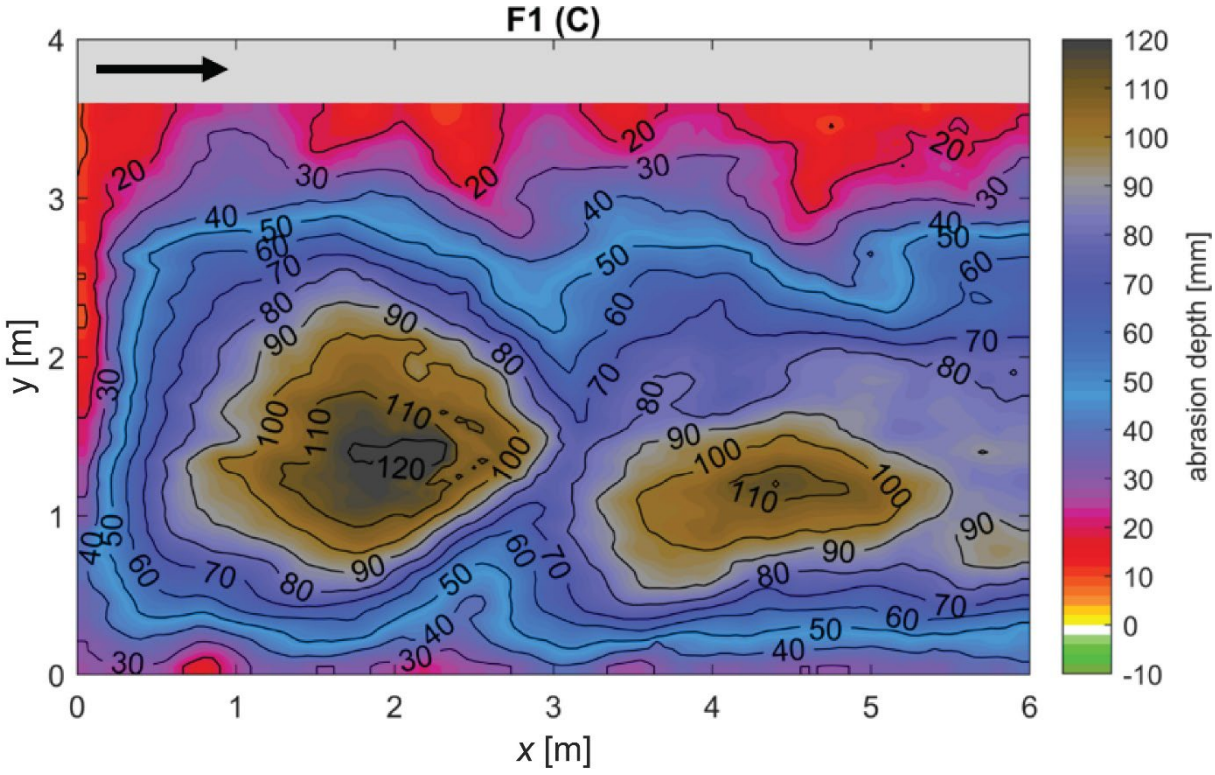

Figure 34: Abrasion topography of test field F1 between 2012 and 2020 in Pfaffensprung SBT with mean abrasion depth of 61 mm.

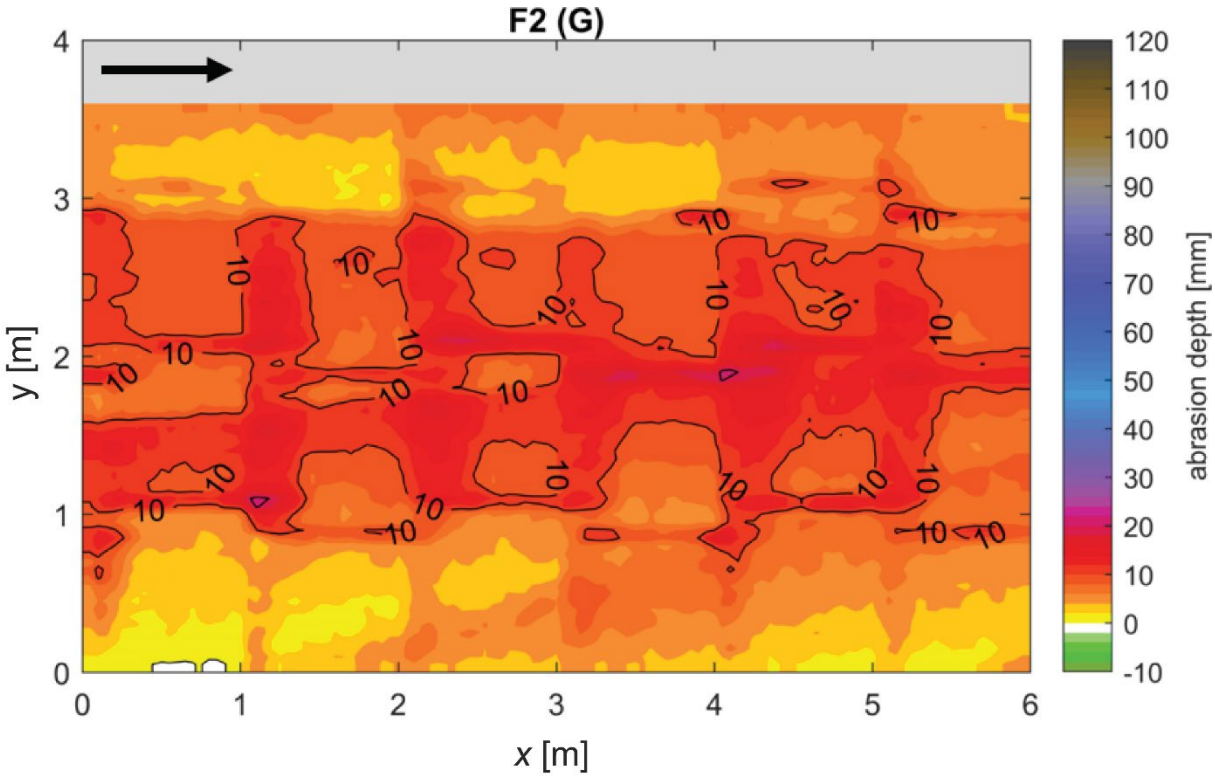

Figure 35: Abrasion topography of test field F2 between 2012 and 2020 in Pfaffensprung SBT with mean abrasion depth of 8 mm.

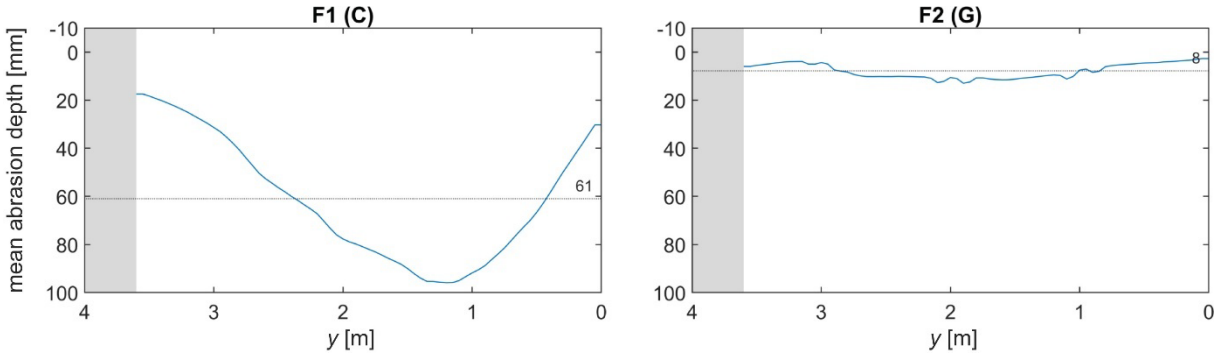

Figure 36: Longitudinally averaged transversal abrasion profiles of test fields F1 and F2 between 2012 and 2020 in Pfaffensprung SBT. The dotted line represents the mean abrasion depth of the test field each.

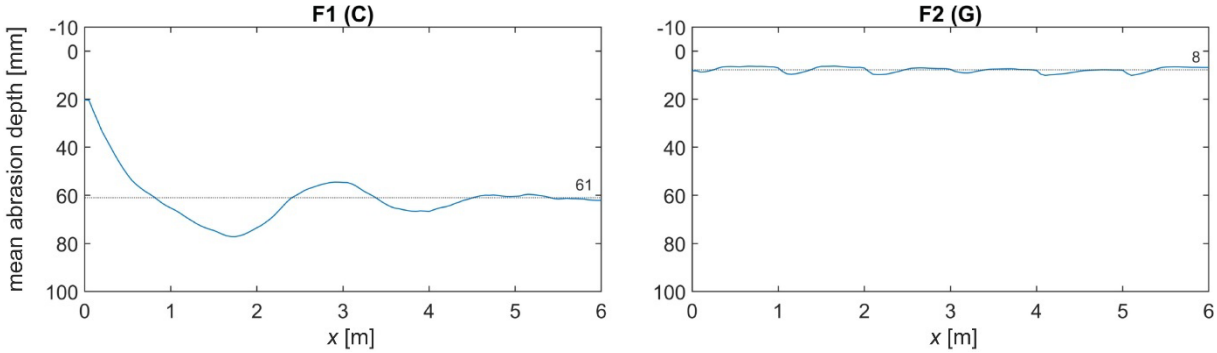

Figure 37: Transversally averaged longitudinal abrasion profiles of test fields F1 and F2 between 2012 and 2020 in Pfaffensprung SBT. The dotted line represents the mean abrasion depth of the test field each.

Figure 38: Picture of test field F1 (Concretem C) during measuring campaign of 7th January 2021 at Pfaffensprung SBT, view against flow direction. The local abrasion at the test field transition is not considered.

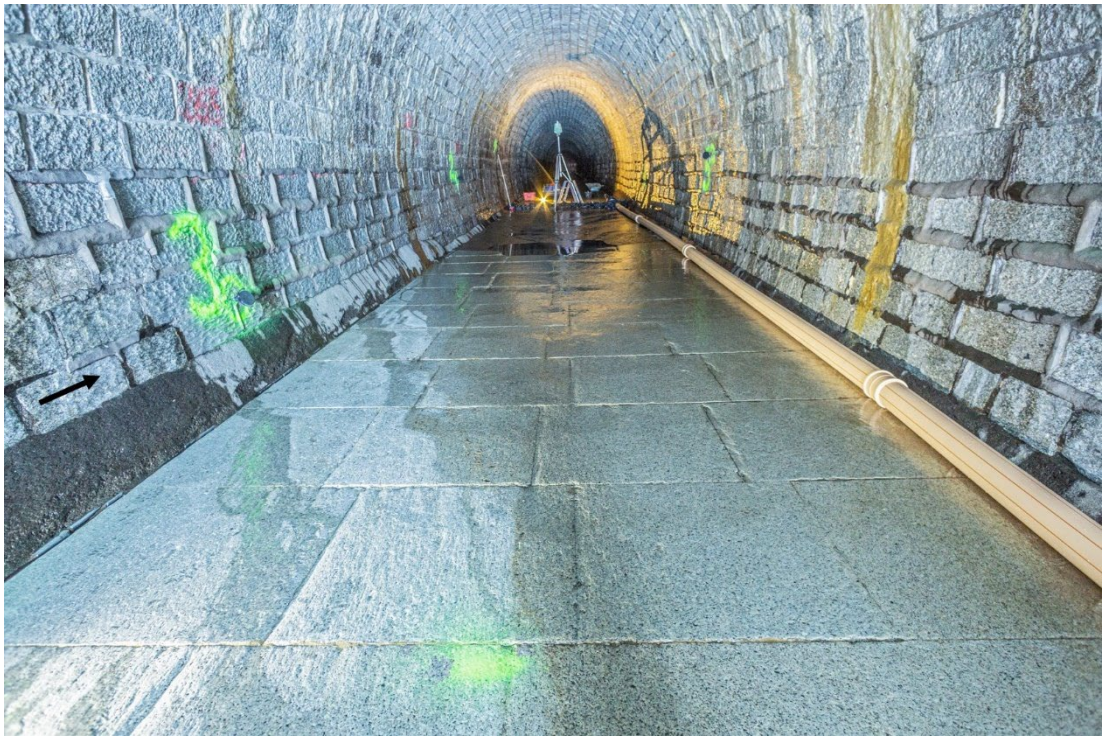

Figure 39: Picture of test field F2 (Granite, G) during measuring campaign of 7th January 2021 at Pfaffensprung SBT, view against flow direction.

3.2.4 Sediment properties

The abrasiveness of the sediments, sampled from the River Reuss in summer 2019, was determined. The particle shapes of the samples are rounded to sub-rounded according to ISO (2013). The results of the XRD are shown in Figure 40. The content of hard minerals, i.e. feldspar and quartz with a Mohs hardness of 6 and 7, respectively, is more than 70%, while soft minerals with a Mohs hardness of less or equal to 2, amount to only 20%, which is opposite to that of the Solis samples (Figure 32). The fraction of hard minerals slightly decreases with increasing particle size, while it is the opposite for the medium and soft minerals (Figure 40b).

The resulting bulk hardness slightly decreases from 5.6 to 5.4 with increasing particle size, indicating a high sediment abrasiveness. Such variations might be attributed to uncertainties and errors of the applied method and analysis and/or physical processes occurring in the catchment and along the river reach. However, the standard deviation of the XRD results is less than 0.16%, which is an order of magnitude below the variation and hence is not at the origin of the variation in mineralogy with particle size. By assuming a spherical particle shape and a bulk density of 2'650 kg/m^3 as rough estimates, the minimum number of particles of 190 results in an error of ±5% at a confidence interval of 95%. Therefore, the results are regarded as representative. Alternative explanation for such variations can be different abrasion rates of different sediment particles and types during transport, as well as various sub-basins with variations in lithology, transport distance, channel morphology and sediment supply rate (Kodama 1994a, b). In general, increasing fractions of hard minerals with increasing particle size would be expected, since hard materials tend to lower diminution and abrasion rates. However, it is reported that different rock types exhibit various abrasion properties, e.g. different dispositions for breaking into smaller pieces of equal sizes, or detachment of smaller pieces like gravel, sand or silt from cobbles, resulting in diminution rates of varying orders of magnitudes despite similar hardness (Kodama 1994a, b).

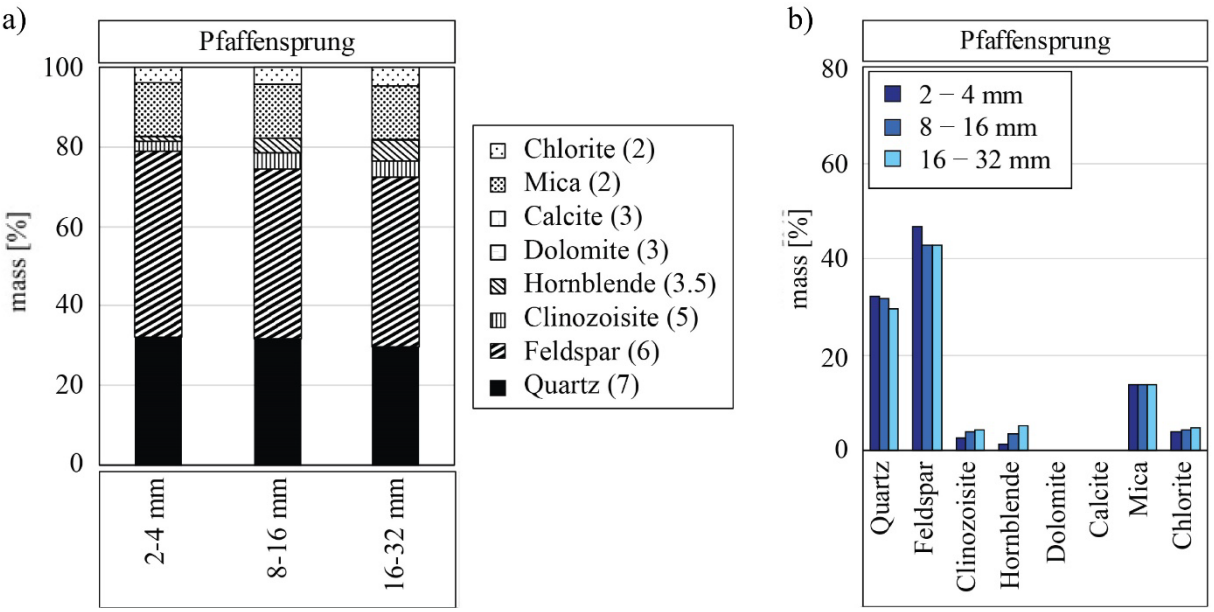

Figure 40: Mineralogical composition of the sediment transported through the Pfaffensprung SBT arranged by a) sediment size and b) mineral type.

3.3 Runcahez SBT

3.3.1 Hydraulic operating conditions

Since no discharge data is available from the Runcahez SBT, the hydraulic conditions in the SBT are determined based on the hydrograph from the gauging station number 2430 (Rein da Sumvitg, Encardens) located 3.5 km upstream and managed by the Federal Office for the Environment (FOEN). To account for the site-specific discharge characteristics, a discharge scaling factor of 4.4 was applied (Müller-Hagmann, 2017). It is assumed that the SBT goes in operation after reaching a discharge of 45 m^3/s for more than 2.5 hours. If this threshold is reached, the entire approach flow is assumed to be bypassed by the SBT till the maximum capacity of the SBT of $Q_{SBT,max}$ = 190 m^3/s is reached. This maximum capacity is achieved after surpassing the design discharge Q_D = 110 m^3/s by changing from free-surface flow conditions to pressurized conditions (Müller-Hagmann, 2017). The excessive water, which cannot be diverted by the SBT is assumed to enter the reservoir. The one- and hundred-year flood discharges in the Rein da Sumvitg are 40 m^3/s and 160 m^3/s, respectively (Axpo, 2011).

The mean discharge through the Runcahez SBT between 2017 and 2020 amounts to 70 m^3/s during bedload transportation, varying between 55 and 93 m^3/s for single years (Table 16). It is assumed that there is bedload transportation in the Rein da Sumvitg already before the SBT goes into operation (see also section 3.3.2). Therefore, there is always bedload transportation during the operation of the SBT. The maximum discharge in the Rein da Sumvitg was measured on 11th August 2019 with 248 m^3/s based on 15 minutes data (63 m^3/s daily mean), thus exceeding the maximum discharge capacity of $Q_{SBT,max}$ = 190 m^3/s. For the period of 2017 to 2020, the SBT was in operation for 57 hours per year on average, varying between 2 and 141 hours for single years. All relevant data are listed in Table 16. Figure 41 shows the time series of discharge (daily resolution) of the SBT for the years 2017 to 2020. Pink vertical lines correspond to the dates of 3D laser scanning of the test fields.

Table 16: Mean and maximum discharge as well as duration of operation between 2017 and 2019 at Runcahez SBT and Rein da Sumvitg. Maximum values are based on 15 minutes data.

Year	Mean SBT discharge during BL transport [m^3/s]	Max SBT discharge, [m^3/s]	Max discharge Rein da Sumvitg [m^3/s]	Duration of SBT operation [h]
2017	55	91	91	21
2018	62	91	91	2
2019	68	190	248	141
2020	93	190	199	62
Average	70			57

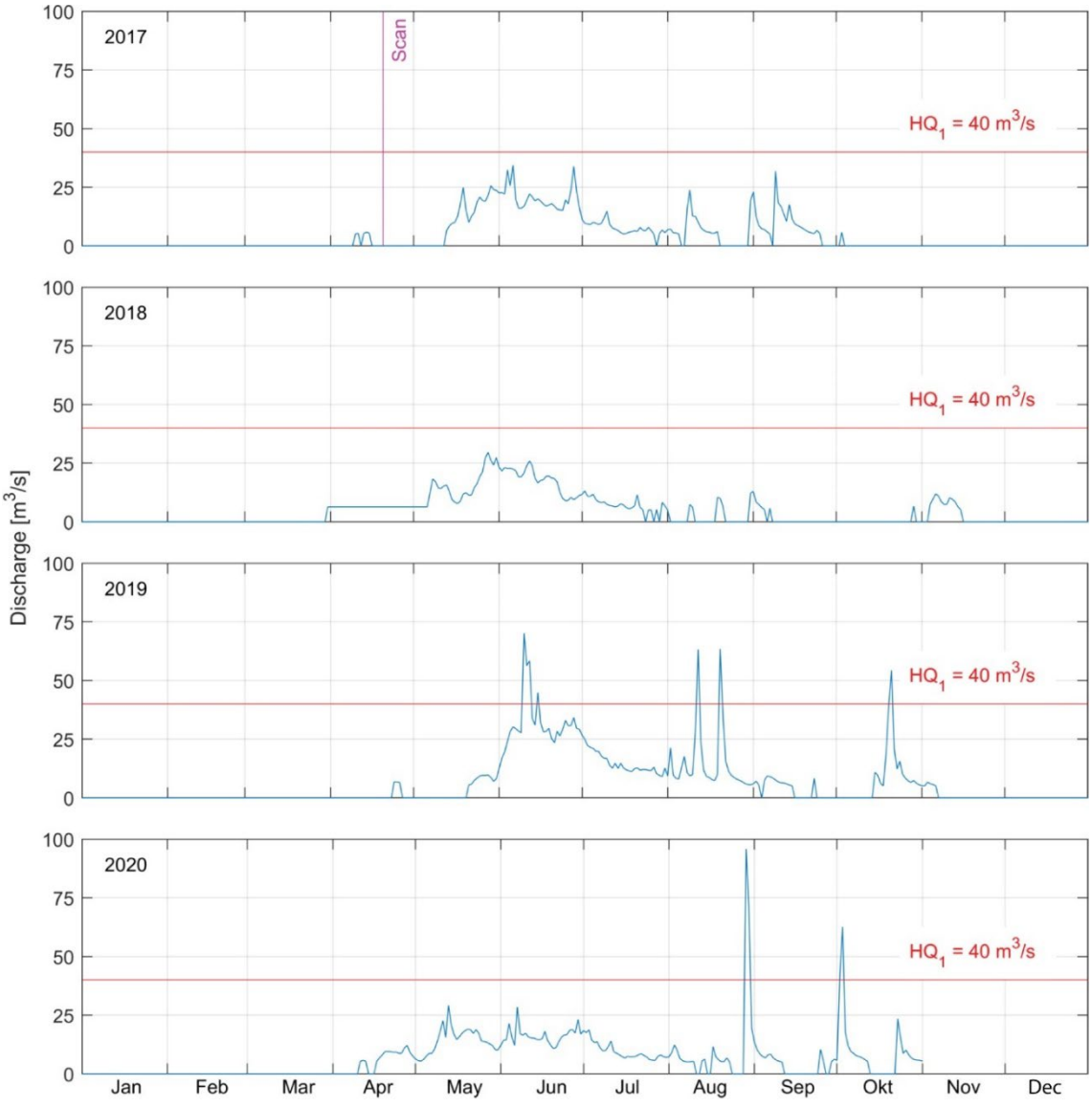

Figure 41: Time series of discharge (daily resolution) of the SBT Runcahez for the years 2017 to 2020. Additionally, the laser scan measuring campaign in April 2017 is indicated as a vertical line.

3.3.2 Sediment transport

As there is no bedload transport measuring system at Runcahez SBT, the bedload transport was estimated based on the effective bedload transport in the Rein da Sumvitg. It is assumed that there is bedload transportation in the Rein da Sumvitg as soon as the critical discharge Q_c = 35 m^3/s is reached (Müller-Hagmann, 2017). The mean annual bedload mass and volume amounts to 17'500 tons and 6'600 m^3, respectively (Table 17). Considering the operation hours of about 57 h (see section 3.3.1), a mean bedload transport rate of 85 kg/s (0.032 m^3/s) is calculated. The assumed bulk density is 2.65 to/m^3.

Table 17: Estimated yearly bedload transport masses and volumes between 2017 and 2020 at Runcahez SBT.

Year	2017	2018	2019	2020	Mean
Bedload transport mass [10^3 to/yr]	5.8	1.0	38.7	24.4	17.5
Bedload transport volume [10^3 m^3/yr]	2.2	0.4	14.6	9.2	6.6

3.3.3 Hydroabrasion

The two-laser scan measuring campaigns were conducted on 20th April 2017 and 4th February 2021, respectively. Table 18 and Figure 42 to Figure 48 show the hydroabrasion between these two measuring campaigns at the five different test fields. At the up- and downstream borders of the test fields, the influence of the laser scanner shadow and the steel beam transition between the different test fields are visible. Therefore, a stripe of 2 m length (3 m for F2) is taken out of the calculations for the mean and maximum abrasion depth at the test field borders.

The largest and lowest spatially averaged abrasion depth of 13 mm and 8 mm were determined at the test fields F2 (RCC, roller compacted concrete) and F4 (SF, steel fiber concrete), respectively. The maximum local abrasion depth of 46 mm was measured at test field F2 (RCC) (Table 18).

The transversal cross-sections of the test fields, averaged over the effective field length of 6 m (5 m for F2), show two incision channels about 15% of the tunnel width away from the sidewalls (Figure 47). The tunnel width to water depth aspect ratios show values greater than 2 (3.8 m width / 1.6 m water depth = 2.375). At such aspect ratios, bed shear stresses are higher close to the tunnel sidewalls where higher abrasion occurs (Auel *et al.*, 2014; Demiral *et al.*, 2020). There is a pronounced abrasion pattern at the left side of the tunnel width in flow direction. This asymmetry can be explained by the upstream bend of the SBT, causing a secondary flow, which moves a part of the sediments towards the inner curve (left side), causing higher abrasion at this side of the test fields.

In longitudinal direction, a wavy abrasion pattern is observed, which is attributed to the hop length of saltating bedload particles (Figure 48). Figure 49 to Figure 53 give a visual impression of the condition of the test fields.

Table 18: Mean and maximum hydroabrasion as well as standard deviation of mean abrasion depth of test fields F0 to F7 between 2017 and 2020 at Runcahez SBT for *x* = [2 or 3,8] m.

Test field	Abrasion [mm]		
	2017 - 2020		
	Mean	Max	Standard dev.
F1 (SC)	11	38	5
F2 (RCC)	13	46	9
F3 (HPC)	9	34	5
F4 (SF)	8	28	5
F5 (PC)	11	37	6

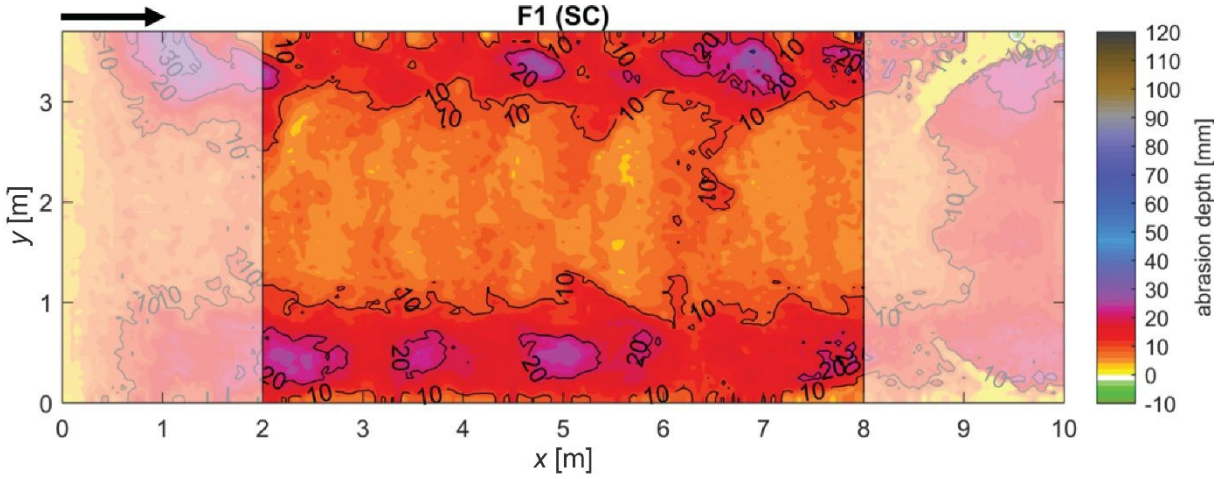

Figure 42: Abrasion topography of test field F0 between 2017 and 2020 in Runcahez SBT with mean abrasion depth of 29 mm.

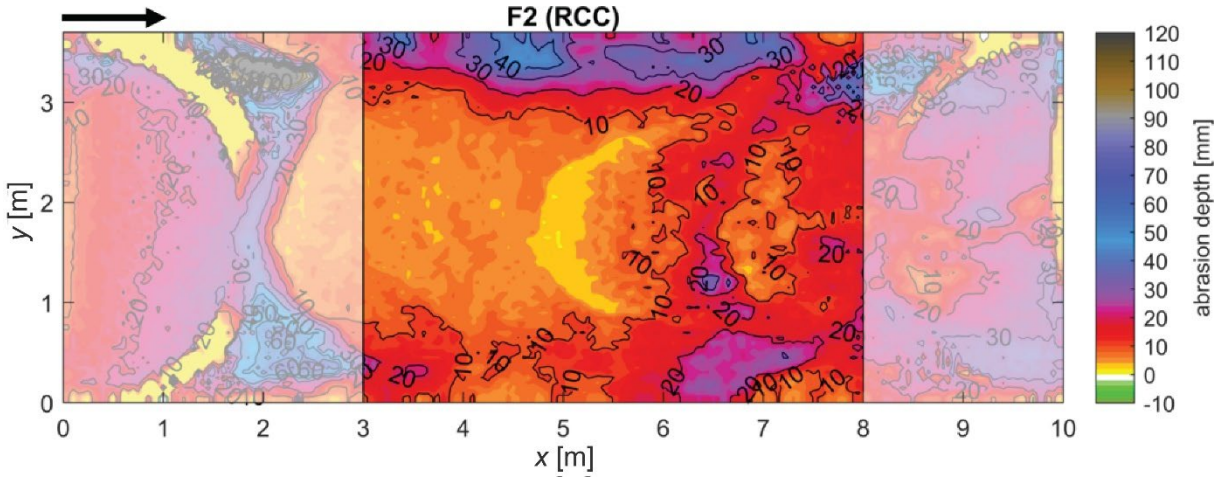

Figure 43: Abrasion topography of test field F0 between 2017 and 2020 in Runcahez SBT with mean abrasion depth of 29 mm.

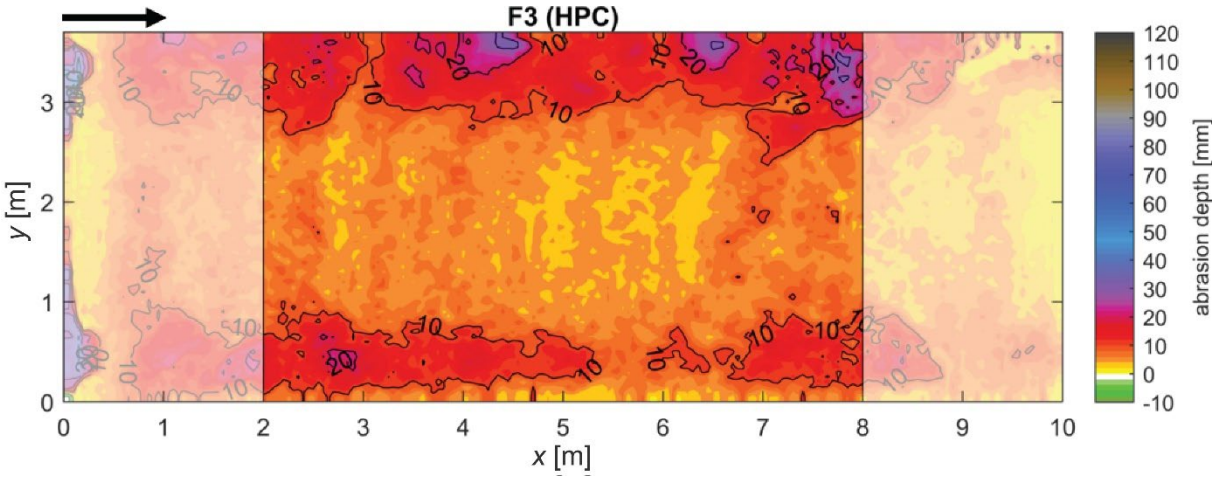

Figure 44: Abrasion topography of test field F0 between 2017 and 2020 in Runcahez SBT with mean abrasion depth of 29 mm.

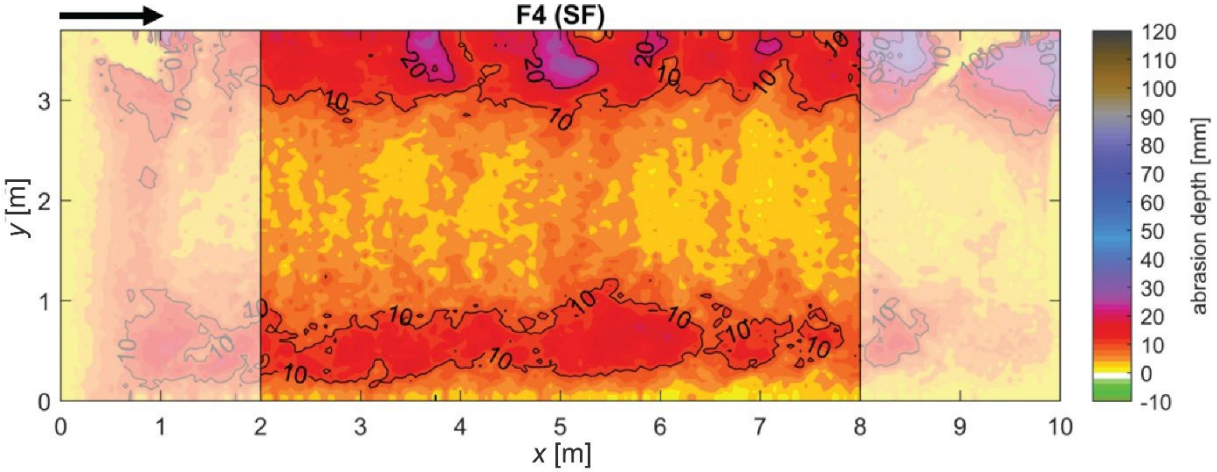

Figure 45: Abrasion topography of test field F0 between 2017 and 2020 in Runcahez SBT with mean abrasion depth of 29 mm.

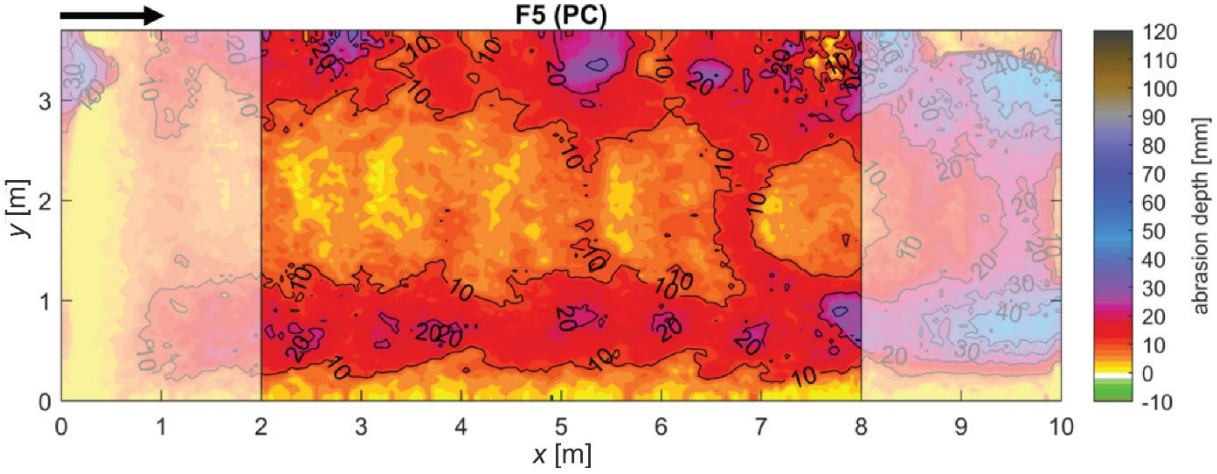

Figure 46: Abrasion topography of test field F0 between 2017 and 2020 in Runcahez SBT with mean abrasion depth of 29 mm.

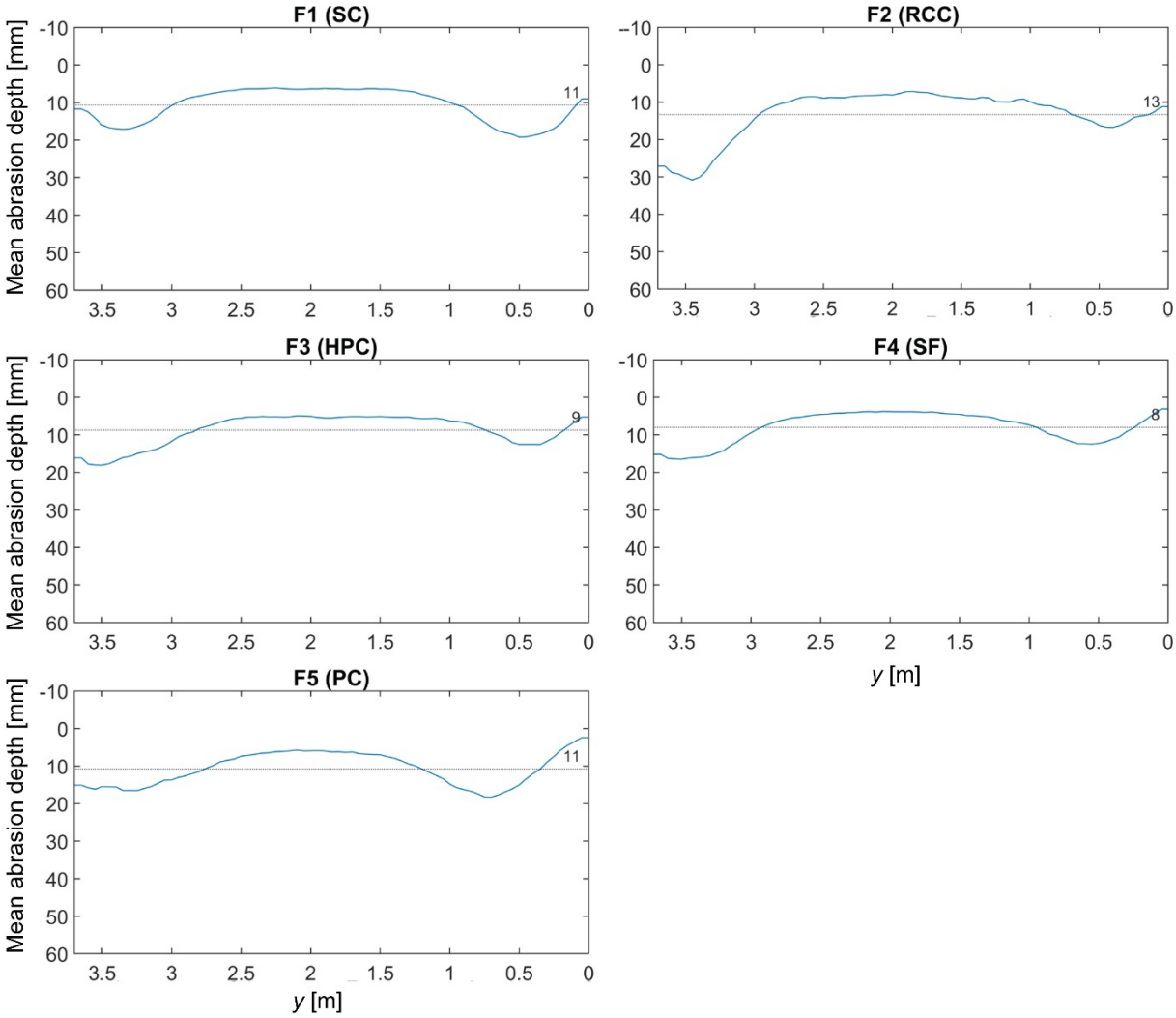

Figure 47: Longitudinally averaged transversal abrasion profiles of test fields F1 to F5 between 2017 and 2020 in Runcahez SBT (view in flow direction). The dotted line represents the mean abrasion depth of the test field each.

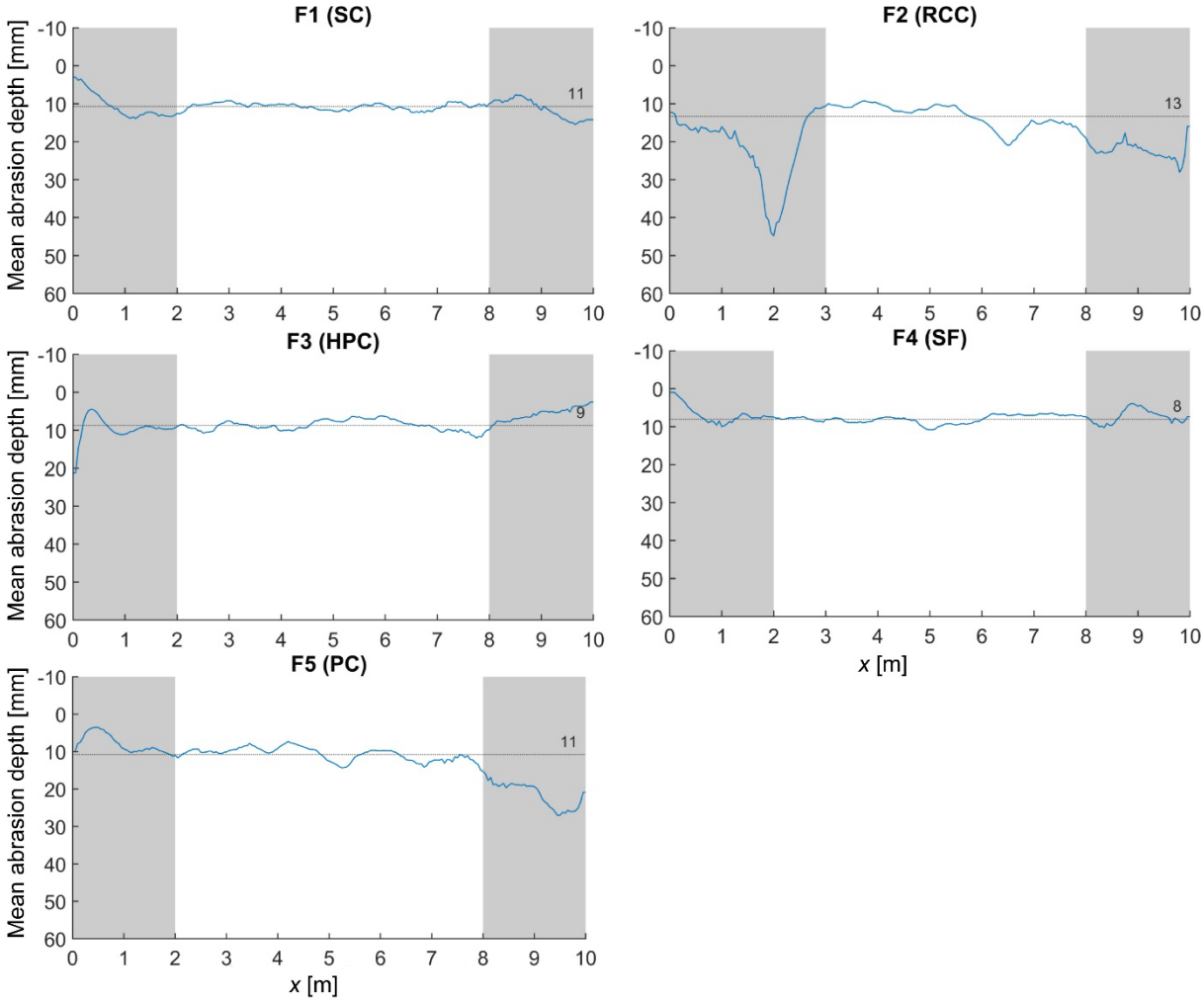

Figure 48: Transversally averaged longitudinal abrasion profiles of test fields F1 to F5 between 2017 and 2020 in Runcahez SBT (flow direction from left to right). The dotted line represents the mean abrasion depth of the test field each. The effective test field length is indicated by the white area.

Figure 49: Picture of test field F1 (Silica fume concrete, SC) during measuring campaign of 4th February 2021 at Runcahez SBT, view in flow direction.

Figure 50: Picture of test field F2 (Roller compacted concrete, RCC) during measuring campaign of 4th February 2021 at Runcahez SBT, view in flow direction.

Figure 51: Picture of test field F3 (High performance concrete, HPC) during measuring campaign of 4th February 2021 at Runcahez SBT, view in flow direction.

Figure 52: Picture of test field F4 (Steel fiber concrete, SF) during measuring campaign of 4th February 2021 at Runcahez SBT, view in flow direction.

Figure 53: Picture of test field F5 (Polymer concrete, PC) during measuring campaign of 4th February 2021 at Runcahez SBT, view in flow direction.

3.3.4 Sediment properties

The abrasiveness of the sediment in the Rein da Sumvitg was determined based on a sample taken and analysed in summer 2019. The sediment particle shape is rounded according to ISO (2013). The results of the XRD are shown in Figure 54. The content of hard minerals, i.e. quartz and feldspar with a Mohs hardness of 7 and 6, respectively, is roughly 60%, while soft minerals with a Mohs hardness of less or equal to 2, amount to only 30%, which is similar to the samples from the Pfaffensprung catchment (compare Figure 40 with Figure 54). As observed at Pfaffensprung, the fraction of hard minerals decreases with increasing particle size.

The bulk hardness decreases from 5.2 to 4.9 with increasing particle size and is slightly below the one of Pfaffensprung, still indicating a rather high sediment abrasiveness. The standard deviation of the XRD analysis is 0.14% and the uncertainty of the samples with a minimum sample size of 220 particles (assuming a spherical particle shape and a bulk density of 2'650 kg/m^3) amounts to ±5% at a confidence interval of 95%. Therefore, the results are regarded as representative, while the observed trend of decreasing hardness with increasing particle size is in the range of these uncertainties. However, effects of different diminution rates of different sediment particles and types as well as various sub-basins with variations in lithology, transport distance, channel morphology and sediment supply rate cannot be excluded and presumably have an impact on the results (Kodama, 1994a, b).

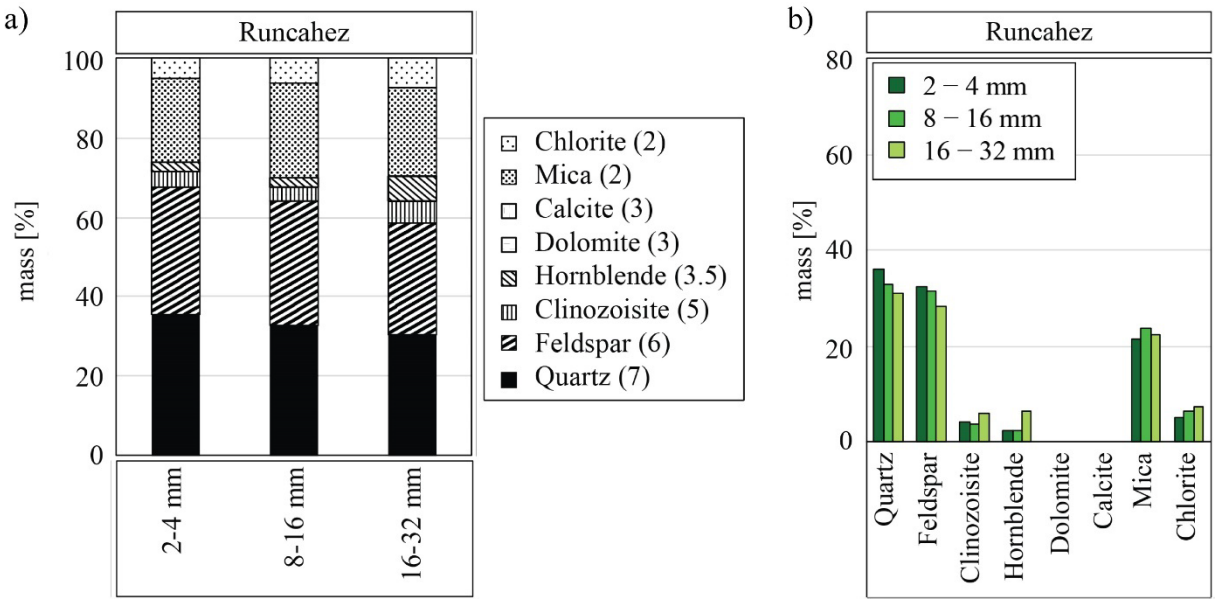

Figure 54: Mineral composition of the sediment transported through the Runcahez SBT arranged by a) sediment size and b) mineral type.

4 Calibration of the enhanced abrasion prediction model (SAMD)

The abrasion prediction model enhanced by Demiral-Yüzügüllü (2021) (SAMD) is calibrated using Demiral's laboratory data and the present data from the hydroabrasion measurements from Pfaffensprung, Runcahez, and Solis SBTs. Table 19 lists the multi-year bedload transport duration, mean discharge during the bedload transport, mean and critical Shields parameters and bedload transport rate per unit width for the studied three SBTs. The material properties of the SBT test fields and the corresponding abrasion depths are summarized in Table 20, while the sediment properties are shown in Table 21. The critical Shields parameters used in the calculations is $\theta_c = 0.013$, which was determined in laboratory experiments for hydraulically rough beds (Demiral-Yüzügüllü, 2021).

Table 19: SBT operation conditions, Shields parameters and bedload transport rates.

SBT (years)	Bedload transport duration [h]	Mean discharge Q_m [m³/s]	Mean Shields parameter θ [-]	Critical Shields parameter θ_c [-]	Bedload transport rate q_s [kg/(m·s)]
Solis (2017-2020)	227	106	0.215	0.013	19.2
Pfaffensprung (2012-2020)	1270	63	0.060	0.013	33
Runcahez (2017-2020)	226	74	0.034	0.013	23

Table 20: Material properties and multi-year mean abrasion depths of SBT test fields in Solis, Pfaffensprung and Runcahez (Demiral-Yüzügüllü, 2021). f_c = compressive strength, f_{tf} = flexural tensile strength, f_{st} = splitting tensile strength, f_y = yield stress, f_u = fracture stress.

SBT (years)	Bed lining material	Density	Strengths			Young's Modulus	Mean abrasion depth
		ρ_s [kg/m^3]	f_c [MPa]	f_{tf} [MPa]	f_{st} [MPa]	Y_M [GPa]	[mm]
Solis (2017-2020)	Normal concrete (NC)	2500 ± 12	105 ± 1.8	11.5 ± 0.5	8.5 ± 0.3	40.7	29
	High strength concrete (HSC)	2474 ± 11	78.9 ± 2.6	12.4 ± 0.5	9.2 ± 0.3	36.2	29
	Low shrinkage concrete (LSC)	2444 ± 20	84.7 ± 2.2	10.8 ± 0.6	8.0 ± 0.4	36.2	35
	Potassium aluminate cement concrete (HAC)	2699 ± 20	86.3 ± 3.4	11.5 ± 0.8	8.5 ±0.5	44.4	10
	Ultra-high-performance concrete (UHPC)	2400 ± 12	187 ± 11	20.9 ± 1.1	15.5 ± 0.7	45.4	29
	Cast basalt plates (CB)	2950	300 - 450	≥ 45	≥ 33	86.6	2
	Steel armouring (SA)	7850	f_y = 235, f_u = 360			210	3
Pfaffensprung (2012-2020)	High strength concrete (C)	2460 ± 30	108 ± 2	15.2 ± 0.4	11.3 ± 0.3	39.7	61
	Granite (G)	2650	260 ± 20	26	28.9	61.8	8
Runcahez (2017-2020)	Silica fume concrete (SC)	2670 ± 16	85.9 ±3.1	11.5 ± 0.6	8.5 ± 2.1	54.1 ± 2.8	11
	High performance concrete (HPC)	2564 ± 52	55.7 ± 4.6	8.3 ± 0.9	6.2 ± 1.0	49.7 ± 1.3	9
	Steel fiber concrete (SF)	2683 ± 16	76.7 ± 2.0	9.6 ± 0.8	7.1 ± 3.0	52.7 ± 4.1	8
	Polymer concrete (PC)	2737 ± 13	95.9 ± 2.3	11.2 ± 0.5	8.3 ± 2.0	52.1 ± 2.7	11
	Roller compacted concrete (RCC)	2366 ± 29	66.8 ± 3.0	14.3 ± 0.9	10.6 ± 1.0	38.5 ± 2.6	13

Table 21: Particle properties in the catchments of Solis, Pfaffensprung and Runcahez SBT.

SBT	Hard mineral content (MH > 7) [%]	Soft mineral content (MH < 2) [%]	Bulk Mohs hardness MH [-]	Particle diameter [m]
Pfaffensprung	> 70	~ 20	5.5	0.25
Runcahez	~ 60	~ 30	5.1	0.23
Solis	~ 20	~ 80*	3.6	0.06

* Soft mineral content, where Mohs hardness < 3.5

Figure 55 shows the abrasion coefficient (k_v) as a function of the splitting tensile strength (f_{st}) for the Demiral-Yüzügüllü's (2021) experimental and SBT field data (Table 22). The mean abrasion coefficient for the field data is $k_v = 4.8 \pm 2.2 \times 10^4$, which is the same as the mean $k_v = 4.8 \pm 1.8 \times 10^4$ of laboratory data (Demiral-Yüzügüllü, 2021), just with slightly higher standard deviation. The scatter of the field data is related to the (i) estimation of bed load transport rate for Pfaffensprung and Runcahez SBTs, (ii) measurement errors in determination of the hydroabrasion depths, and (iii) input parameter calculations based on the initial flow conditions and the initial invert lining conditions. Despite all these effects, the field data are still in a reasonable range similar to the laboratory data scatter.

Overall, both field and laboratory data match well indicating no splitting tensile strength effect on k_v as theoretically expected. Only the k_v parameter for the ultra-high-performance concrete (UHPC) of Solis SBT seems to be an outlier presenting a lower value compared to the other data group. Although UHPC is a higher strength concrete compared to the other types of concretes in the Solis SBT, the abrasion depth of UHPC is significant, revealing approximately the same value with the normal concrete (NC) of considerably lower strength (Table 20). The worse hydroabrasion performance of UHPC compared to other concretes may be related to its implementation in the field. Additionally, UHPC consists of a high volume of hardened cement paste, which decreases the hardness of the bed lining material (personal communication with Dr. Frank Jacobs, 2021). The low bed lining material hardness may also be the reason of the high abrasion depths in UHPC. Overall, the comparison between the laboratory data and SBT data demonstrates that the laboratory results can be upscaled to the prototype scale.

Demiral-Yüzügüllü's (2021) and the present hydroabrasion measurements reveal that for homogeneous bed lining materials, such as foam and well-poured concrete, one or two continuous incision channels develop, depending on the channel aspect ratio (channel width to water dept ratio). Since abrasion depths vary across the channel, the mean, i.e., spatially averaged abrasion depth, solely is not a sufficient parameter to describe the abrasion distribution and pattern. The relation between the mean abrasion depth (Eq. 14 in section 2) and its standard deviation is $\sigma = 0.51 \times h_a + 0.31 \times h_a = 0.82 \times h_a$ (h_a = mean abrasion depth) by considering the present and Demiral-Yüzügüllü's (2021) data, which allows to determine the minimum and maximum abrasion. For engineering application of the SAMD model, Demiral-Yüzügüllü (2021) recommends $h_{a,max} = h_a + 2\times\sigma = 2.64 \times h_a$ for maximum abrasion depth and $h_{a,min} = 0$.

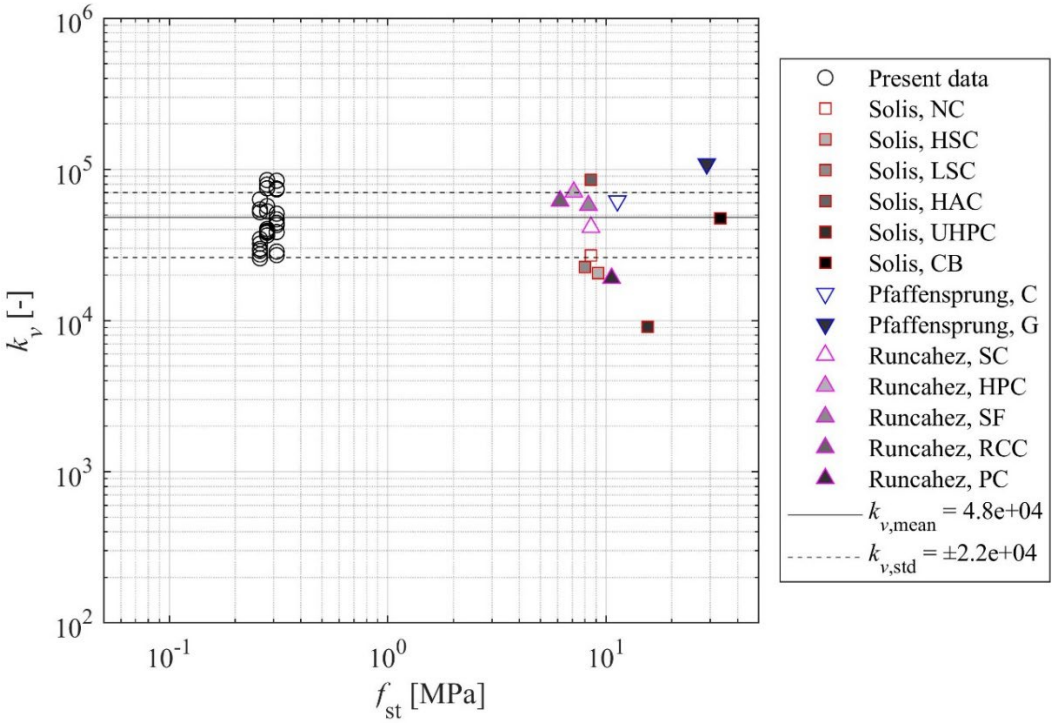

Figure 55: Abrasion coefficient (k_v) versus splitting tensile strength (f_{st}) of the laboratory data of Demiral-Yüzügüllü, 2021 and field data of the SBTs.

Table 22: Abrasion coefficient (k_v) and splitting tensile strength (f_{st}) of test field data.

SBT	Bed lining material	k_v [-]	f_{st} [MPa]
Solis	Normal concrete (NC)	26’640	8.5
	High strength concrete (HSC)	20’630	9.2
	Low shrinkage concrete (LSC)	22’520	8.0
	Potassium aluminate cement concrete (HAC)	85’290	8.5
	Ultra-high-performance concrete (UHPC)	9’111	15.5
	Cast basalt plates (CB)	47’650	33.3
Pfaffen sprung	High strength concrete (C)	61’828	11.3
	Granite (G)	108’647	28.9
Runcahez	Silica fume concrete (SC)	41’450	8.5
	High performance concrete (HPC)	70’818	7.1
	Steel fiber concrete (SF)	57’867	8.3
	Polymer concrete (PC)	19’077	10.6
	Roller compacted concrete (RCC)	61’855	6.2

5 Engineering application of the SAMD model

The enhanced saltation abrasion model (SAMD, Eq. 14) requires the input parameters listed in Table 23 to predict the vertical abrasion rate per unit time, A_r (m/s). Table 23 also shows the recommended methods to measure and equations to predict these parameters if their direct measurements are not possible.

Table 23: The input parameters of SAMD and methods and predictive equation to determine parameters

Input parameters for SAMD		**Methods to determine parameter**	**Predictive equation**
k_v [-]	Non-dimensional hydroabrasion coefficient	$4.8 \pm 2.2 \times 10^4$, (see chapter 4)	
Y_M [Pa]	Young's modulus of invert material	Direct strength test	• Eq. (18) for concrete and natural bedrock with $f_{c,cyl}$ > 40 MPa • Eq. (19) for weak mortar mixtures, soft bedrocks
f_{st} [Pa]	Splitting tensile strength of invert material	Indirect (Brazilian) tensile strength test	• Eq. (20) for concrete and natural bedrock with $f_{c,cyl}$ > 4 MPa • Eq. (21) for weak mortar mixtures, soft bedrocks
s [-]	Non-dimensional specific density of sediment	Laboratory measurement or 2.65 for natural sediment particles (Fredsøe and Deigaard, 1992)	
T^* [-] = $(\theta - \theta_c)$-1	Excess transport stage requiring particle diameter, d_{50} and friction velocity, U_*		
d_{50} [m]	Particle diameter	Sieve analysis	
U_* [m/s]	Friction velocity		• Eq. (22), using channel bed slope in uniform flows • Eq. (22), using energy line slope in non-uniform flows • Backwater curve calculations • Using log-law if velocity measurement exists
q_s [kg/(m·s)]	Unit gravimetric sediment transport rate	Swiss Plate Geophone System for direct measurement	• See details in Section 4.1.3 in Müller-Hagmann (2017)
q_s^*[kg/(m·s)]	Unit gravimetric sediment transport capacity		For fixed beds • Eq. (12) (Demiral-Yüzügüllü, 2021) • Eq. (23) (Pedroli, 1963)

MH [-] MH_B [-]	Bulk Mohs hardness of sediment Mohs hardness of invert materials	Mohs hardness kit or XRD analysis

Noguchi *et al*. (2009) developed the following practical equation to predict Young's modulus, Y_M of concrete or natural bedrock with cylindrical compressive strength between 40 MPa < $f_{c,cyl}$ < 160 MPa:

$$Y_M = 3.35\times10^4 k_1 k_2 \sqrt[3]{\left(\frac{f_{c,cyl}}{60}\right)\left(\frac{\rho_m}{2400}\right)^2} \quad \text{for } 40 < f_{c,cyl} < 160\,\text{MPa} \qquad \text{[MPa]} \qquad (18)$$

where $f_{c,cyl} = 0.8f_c$, ρ_m = material density [kg/m³], k_1 = correction factor depending on the type of coarse aggregates, and k_2 = correction factor depending on the mineral admixtures in the concrete. The correction factors $k1$ and $k2$ vary in a range of $0.90 \le k_1 \le 1.21$, and $0.95 \le k_2 \le 1.10$, respectively. Demiral-Yüzügüllü (2021) developed the following equation to predict Y_M of weak mortar mixtures and soft bedrocks:

$$Y_M = 2014.5 f_c^{0.981} \qquad \text{[MPa]} \qquad (19)$$

Arıoğlu *et al*. (2006) proposed the following equation to estimate the splitting tensile strength based on the compression strength for concretes:

$$f_{st} = 0.387 f_{c,cyl}^{0.63} \quad \text{for } 4 \le f_{c,cyl} \le 120\,\text{MPa} \qquad \text{[MPa]} \qquad (20)$$

For weak mortar mixtures and soft bedrocks, Demiral-Yüzügüllü (2021) proposes the following equation for f_{st}:

$$f_{st} = 0.109 f_c^{0.758} \qquad \text{[MPa]} \qquad (21)$$

Friction velocity, also called "shear velocity", is a fictive velocity representing the bed shear stress in velocity units. In uniform flows, the flume average friction velocity U_* is calculated with the following equation using the channel bed slope:

$$U_* = \sqrt{gR_hS_b} \qquad \text{[m/s]} \qquad (22)$$

where $R_h = A_w/P_w$ = hydraulic radius with A_w and P_w = wetted area and perimeter, respectively, and S_b = channel bed slope. In non-uniform flows, the friction velocity U_* can be calculated using the energy line slope S_e instead of S_b in Eq. (22).

Unit gravimetric sediment transport capacity, q_s^* can be determined using the following equation developed by Pedroli (1963):

$$q_s^* = 14.5\frac{\tau_b^{8/5} D^{1/5} g^{3/5}}{\rho_s^{3/5} \nu^{1/5}} - 23.2\rho_s \nu \qquad \text{[kg/(m·s)]} \qquad (23)$$

where τ_b = bed shear stress = $U_*^2\rho$, ρ_s = particle density, ν = kinematic viscosity of water.

For engineering application of SAMD to estimate abrasions rates, the following recommendations are made based on the present results and the laboratory results of Demiral-Yüzügüllü (2021):

For a hydraulic structure prone to hydroabrasion, the properties of the sediment particles and invert material, the hydraulic conditions, sediment transport rates and transport capacity should be determined or estimated as precisely as possible using the methods and equations presented in Table 23.

The standard deviation of the hydroabrasion coefficient k_v should be considered when calculating a range of abrasion rates. By this way, the prediction range (average A_r (k_v = 4.8 × 10^4), minimum $A_{r,min}$ (k_v = 7.0 × 10^4) and maximum $A_{r,max}$ (k_v = 2.6 × 10^4)) can be calculated, and the uncertainties caused by incorrect estimations of the model input parameters are considered.

For homogeneous invert materials such as concrete and natural stone pavers, incision channels are expected to form, as observed in three Swiss SBTs. Therefore, the mean, i.e., spatially averaged, abrasion depth alone is not sufficient to represent the abrasion distribution. The maximum abrasion depth should be calculated as described in section 4. In doing so, the 95th percentile, represented by twice the standard deviation, is recommended as a proxy for the maximum ($h_{a,max} = h_a + 2\times\sigma = 2.64 \times h_a$).

Hydroabrasion development should be monitored and mapped on a regular basis, e.g., after the yearly flood season. By doing so, the measured abrasion depths can be compared to the predictions and potential deviations are recognized at an early stage to adapt maintenance and refurbishment intervals if necessary.

Prior to new SBT constructions or refurbishments of the invert materials, the expected abrasion rates should be determined using SAMD for different types of bed lining materials, e.g., concrete, granite, cast basalt, or natural bedrocks. Then, an economical assessment based on net present values which account for the investment costs, construction lifespan, expected abrasion damages and maintenance costs should be made to select the most cost-effective invert material.

6 Conclusions

The present pilot and demonstration project deals with an important engineering problem of hydroabrasion at hydraulic structures, particularly at sediment bypass tunnels. In this project, the abrasion resistance of various invert materials was quantified by performing annual 3D laser scanning and monitoring hydraulic conditions and sediment transport between 2017 and 2021 at three Swiss SBTs, namely Solis, Pfaffensprung and Runcahez, subject to hydroabrasive wear. In addition, a Swiss Geophone Plate System (SGPS) installed at the outlet of the Solis SBT was calibrated in 2021 and a new calibration coefficient as a function of particle diameter and overlapping parameter of z_p was determined from the present and previous calibration data.

The results show that the hydraulics of SBT flows affect the abrasion pattern of the tunnel inverts. In the straight section of Solis SBT, where the aspect ratio of the tunnel width to the flow depth is less than 2 (i.e., 1.7), sediment transport and hydroabrasion concentrated at the centre of the tunnel with maxima between 125% and 175% of the mean abrasion depth across the tunnel width due to the strong secondary currents. When the aspect ratio is larger than 2, as in Runcahez SBT with 2.375, the sediment transport and hydroabrasion concentrate towards the tunnel walls. At Pfaffensprung SBT, the second type of secondary currents occured due to a tunnel bend, concentrating sediment transport at the inner side of the bend and in the straight section further downstream, where the concrete test field was installed. This resulted in stronger hydroabrasion at these locations. However, this abrasion pattern was not observed on the granite test field, installed downstream of the concrete test field. At the granite test field, higher abrasion depths were determined at the joints of the granite plates. A similar pattern was observed on the basalt plates in the Solis SBT.

Granite, cast basalt and steel plates as well as potassium aluminate cement concrete show a good performance to withstand sediment-laden flows and hydroabrasive processes at Solis and Pfaffensprung SBTs. At the Runcahez SBT, the steel fiber concrete shows the best performance. The hydroabrasive resistance of the Ultra High-Performance Concrete in Solis SBT was poor compared to other invert materials with lower compression strengths, which might be related to its poor implementation in the field. The abrasion resistance of granite with f_c = 260 MPa is roughly 7.5 times higher than that of high-strength concrete with f_c = 108 MPa at Pfaffensprung SBT.

Sediment properties such as shape and mineral composition change from catchment to catchment. Sediments in the Solis catchment are relatively soft with a bulk Mohs hardness of between 3.5 and 3.7, whereas sediments in Pfaffensprung and Runcahez are harder with a bulk Mohs hardness of 5.4-5.6 and 4.9-5.2, respectively. Such differences in sediment hardness affect hydroabrasion significantly.

A mechanistic saltation abrasion model was enhanced at VAW by including new sediment trajectory equations and particle saltation probability equations for rough beds, as well as particle hardness, and cover effect equations (Demiral-Yüzügüllü 2021) into the existing model. This model (SAMD) was developed with laboratory data and calibrated with the present data from the Swiss SBTs. A mean abrasion coefficient value of $k_v = (4.8 \pm 2.2) \times 10^4$ was determined. The results revealed that this quasi-constant abrasion coefficient is applicable for brittle materials independent of the flow conditions, material strength, and particle properties. The standard deviation of the abrasion coefficient, i.e., 2.2×10^4, is caused by the uncertainties in the input parameters such as splitting tensile strength, Young's modulus, and bedload estimation in the field. The enhanced saltation abrasion model SAMD is applicable for both the laboratory and field scales, such as hydraulic structures and steep bedrock rivers, indicating that the laboratory findings can be upscaled to the prototype scale.

7 Outlook and next steps

In the present field study, the flow characteristics, sediment transport, and hydroabrasion of different invert materials was investigated at three Swiss SBTs and an enhanced mechanistic saltation abrasion model (SAMD) was calibrated to predict abrasion rates in steep bedrock rivers and at hydraulic structures. The SAMD model performs well in the prediction of hydroabrasion in laboratory and field conditions. However, there is still room to improve the SAMD by conducting research on the following topics:

- The particle hardness coefficient k_H for relative hardness ratios $MH/MH_B < 1$ should be further investigated using different lithologies and different bed lining materials. Therefore, more data is needed to improve this coefficient in the regions where the particle hardness of the sediment particles MH is lower than the invert material hardness MH_B.
- The flow characteristics, particle motion, and hydroabrasion development should be investigated systematically in curved channels, which represent bends of SBTs and meandering sections of rivers.
- Hydroabrasion mechanics and patterns at the joints between invert materials should be further investigated and included in the model.

The results of the present project will be published in a peer-reviewed journal and presented in an international conference or workshop.

8 National and international cooperation

In this project, VAW conducted field investigation on hydroabrasion together with its partners between 2017 and 2021. The partners were the operators of Pfaffensprung SBT (SBB), Solis (ewz) and Runcahez (Axpo). They supported the project with their staff during the field campaigns and provided the operation data to VAW. Furthermore, Prof. Robert Boes and Dr. Ismail Albayrak organized a meeting with SBB on 10th December 2021, presented and discussed the project results with the responsible engineers and project managers from SBB and visited the Pfaffensprung SBT. VAW and SBB decided to be in contact for possible additional field measurement campaign in the future before

they remove the concrete test field. VAW will organize similar meetings with ewz and Axpo in 2022 to present the project results and discuss potential future collaborations on this topic.

9 References

Albayrak, I., Müller-Hagmann, M., Boes, R. M. (2017). Calibration of Swiss Plate Geophone System for bedload monitoring in a sediment bypass tunnel. Proc. *2nd International Workshop on Sediment Bypass Tunnels* (T. Sumi, ed.), Kyoto University, Japan.

Arıoğlu, N., Girgin, Z. C., & Arıoğlu, E. (2006). Evaluation of ratio between splitting tensile strength and compressive strength for concretes up to 120 MPa and its application in strength criterion. *ACI Materials Journal*, *103*(1), 18–24.

Auel, C. (2014). Flow characteristics, particle motion and invert abrasion in sediment bypass tunnels. *VAW-Mitteilungen* 229 (R. Boes, ed.), ETH Zurich, Switzerland.

Auel, C., Boes, R. M. (2011). Sediment bypass tunnel design - review and outlook. Proc. *ICOLD Symposium "Dams under changing challenges"* (A. J. Schleiss & R. M. Boes, eds.), 79th Annual Meeting, Lucerne, Switzerland: 403-412.

Auel, C., Albayrak, I., Boes, R. M. (2014). Turbulence characteristics in supercritical open channel flows: Effects of Froude number and aspect ratio. Journal of Hydraulic Engineering 140 (4): 04014004_04014001-04014004_04014016.

Auel, C., Albayrak, I., Sumi, T., & Boes, R. M. (2017a). Sediment transport in high-speed flows over a fixed bed: 1. Particle dynamics. *Earth Surface Processes and Landforms*, *42*(9), 1365–1383. https://doi.org/10.1002/esp.4128.

Auel, C., Albayrak, I., Sumi, T., & Boes, R. M. (2017b). Sediment transport in high-speed flows over a fixed bed: 2. Particle impacts and abrasion prediction. *Earth Surface Processes and Landforms*, *42*(9), 1384–1396. https://doi.org/10.1002/esp.4132.

Axpo (2011). Fragebogen Sedimentumleitstollen Runcahez ('Questionnaire about Runcahez sediment bypass tunnel'). Filled by E. Degonda. Laboratory of Hydraulics, Hydrology and Glaciology (VAW), ETH Zurich, Switzerland (in German, unpublished).

Boes, R. M., Auel, C., Hagmann, M., Albayrak, I. (2014). Sediment bypass tunnels to mitigate reservoir sedimentation and restore sediment continuity. Proc. *Riverflow 2014* (A. J. Schleiss *et al.*, eds.), Lausanne, Switzerland: 221-228.

Chiari, M., Berktold, M., Jäger, G., Hübel, J. (2016). Geschiebemessstelle im Suggadinbach (Vorarlberg) ('Bedload monitoring station at Suggadinbach (Vorarlberg)'). Feststofftransport und Sedimentmanagement. Verein der Diplomingenieure der Wildbach und Lawinenverbauung Österreichs: 50-58 (in German).

Demiral, D., Boes, R.M., Albayrak, I. (2020). Effects of Secondary Currents on Turbulence Characteristics of Supercritical Open Channel Flows at Low Aspect Ratios. *Water*, 12 (11), 3233, https://doi.org/10.3390/w12113233.

Demiral-Yüzügüllü, D. (2021). Hydro-abrasion processes and modelling at hydraulic structures and steep bedrock rivers. *VAW-Mitteilungen* 261 (R. Boes, ed.), Also published as a Doctoral Thesis, ETH Zurich, Switzerland, https://doi.org/10.3929/ethz-b-000509044.

Dhont, B. E. M., Rousseau, G., Ancey, C. (2017). Continuous monitoring of bedload transport in a laboratory flume using an impact sensor. Journal of Hydraulic Engineering 143 (6).

Engel, P. A. (1978). Impact wear of materials. *Journal of Applied Mechanics, 45*(2), 458.

Felix, D. (2017) Experimental investigation on suspended sediment, hydro-abrasive erosion and efficiency reductions of coated Pelton turbines. *VAW-Mitteilungen* 238 (R. Boes, ed.), Also published as a Doctoral Thesis. Nr. 24145, ETH Zurich. ETH Zurich, Switzerland.

Fredsøe, J., Deigaard, R. (1992). *Mechanics of coastal sediment transport* (Vol. 3, p. 369). World Scientific.

Harada, M., Terada, M., Kokubo, T. (1997). Planning and hydaulic design of bypass tunnel for sluicing sediments past Asahi reservoir. *19th ICOLD Congress*, Florence, Italy: 509-539.

ISO (2013). 14689:2018-5: Geotechnical Investigation and Testing: Identification and Classification of Soil. Identification and DescriptionInternational Organization for Standardization. International Organization for Standardization.

Kodama, Y. (1994a). Downstream changes in the lithology and grain size of fluvial gravels, the Watarase River, Japan; evidence of the role of abrasion in downstream fining. *Journal of Sedimentary Research* 64 (1a): 68-75.

Kodama, Y. (1994b). Experimental study of abrasion and its role in producing downstream fining in gravel-bed rivers. *Journal of Sedimentary Research* 64 (1a): 76-85.

Koshiba, T., Auel, C., Tsutsumi, D., Kantoush, S., Sumi, T. (2018). Application of an impact plate - bedload transport measuring system for high-speed flows. International Journal of Science and Research, 33(1): 35-46, https://doi.org/10.1016/j.ijsrc.2017.12.003.

Morach, S. (2011). Geschiebemessung mittels Geophonen bei hohen Fliessgeschwindigkeiten - Hydraulische Modellversuche ('Bedload transport measurement at high flow velocities - hydraulic model tests'). Master Thesis, VAW, ETH Zurich, Switzerland (in German, unpublished).

Morris, G. L., Fan, J. (1998). Reservoir Sedimentation Handbook. New York, United States., McGraw-Hill Book Co.

Müller-Hagmann, M. (2017). Hydroabrasion in high-speed sediment-laden flows in sediment bypass tunnels. *VAW-Mitteilungen* 239 (R. Boes, ed.), Also published as a Doctoral Thesis. No. 24291, ETH Zurich, Switzerland.

Müller-Hagmann, M., Albayrak, I., Auel, C., Boes, R.M. (2020). Field investigation on hydroabrasion in high-speed sediment-laden flows at sediment bypass tunnels. *Water*, 12(2), 469, https://doi.org/10.3390/w12020469.

Noguchi, T., Tomosawa, F., Nemati, K. M., Chiaia, B. M., & Fantilli, A. P. (2009). A practical equation for elastic modulus of concrete. *ACI Structural Journal*, 7.

Pedroli, R. (1963). Trasporto di materiale solido in canali a fondo fisso e liscio ('Sediment transport in channels with a fixed and smooth bed') [Doctoral Thesis]. ETH Zurich (in Italian).

Rickenmann, D., Turowski, J. M., Fritschi, B., Klaiber, A., Ludwig, A. (2012). Bedload transport measurements at the Erlenbach stream with geophones and automated basket samplers. Earth Surface Processes and Landforms 37 (9): 1000-1011.

Rickenmann, D., Turowski, J. M., Fritschi, B., Wyss, C., Laronne, J., Barzilai, R., Reid, I., Kreisler, A., Aigner, J., Seitz, H., Habersack, H. (2013). Bedload transport measurements with impact plate geophones: comparison of sensor calibration in different gravel-bed streams. Earth Surface Processes and Landforms 39 (7): 928-942.

Sklar, L. S., Dietrich, W. E. (2001). Sediment and rock strength controls on river incision into bedrock. *Geology* 29 (12): 1087-1090.

Sklar, L. S., Dietrich, W. E. (2004). A mechanistic model for river incision into bedrock by saltating bed load. *Water Resources Research* 40 (6). DOI: W06301 10.1029/2003wr002496.

Sklar, L. S., Dietrich, W. E. (2012). Correction to "A mechanistic model for river incision into bedrock by saltating bed load". *Water Resources Research* 48 (6). DOI: W06301/10.1029/2003wr002496.

Sumi T., Okano M., Takata Y. (2004). Quantitative evaluation of a bypass tunnel to prevent reservoir sedimentation. *Journal of Japan Society of Civil Engineers, Advances in River Engineering 10*: 197-202 (In Japanese).

Turowski, J. M., Böckli, M., Rickenmann, D., Beer, A. R. (2013). Field measurements of the energy delivered to the channel bed by moving bed load and links to bedrock erosion. Journal of Geophysical Research: Earth Surface 118 (4): 2438-2450.

VAW (1992). Flussmorphologie des Mittellaufes zwischen Göschenen und Amsteg ('River morphology of the middle reaches between Göschenen and Amsteg'). *Report No. 4014/3967*, VAW, ETH Zurich, Switzerland (in German, unpublished).

Xie, J., Tamaki, J. (2007). Parameterization of micro-hardness distribution in granite related to abrasive machining performance. *Journal of Materials Processing Technology* 186 (1-3): 253-258.

Wyss, C. R. (2016). Sediment transport measurements with geophone sensors. VAW-Mitteilungen 234 (R. Boes, ed.), Also published as a Doctoral Thesis. Nr. 23353, ETH Zurich. ETH Zurich, Switzerland.

Wyss, C. R., Rickenmann, D., Fritschi, B., Turowski, J. M., Weitbrecht, V., Boes, R. M. (2015). Measuring bedload transport rates by grain-size fraction using the swiss plate geophone signal at the Erlenbach. Journal of Hydraulic Engineering 142 (5): 04016003.

Wyss, C. R., Rickenmann, D., Fritschi, B., Turowski, J. M., Weitbrecht, V., Boes, R. M. (2016a). Laboratory flume experiments with the Swiss plate geophone bed load monitoring system: 1. Impulse counts and particle size identification. Water Resources Research 52 (10): 7744-7759.

Wyss, C. R., Rickenmann, D., Fritschi, B., Turowski, J. M., Weitbrecht, V., Travaglini, E., Bardou, E., Boes, R. M. (2016b). Laboratory flume experiments with the Swiss plate geophone bed load monitoring system: 2. Application to field sites with direct bed load samples. Water Resources Research 52 (10): 7760-7778.

10 Appendix

10.1 Solis SBT

10.1.1 Characteristics of major rain events and SBT operation at Solis SBT

Table 24: Characteristics of major rain events and SBT operation in 2017 and 2018 at Solis SBT.

		06.06.2017	01.06.2018	12.09.2018	08.10.2018
Start of BL transport		06.06.2017 14:00	01.06.2018 11:00	12.09.2018 21:00	08.10.2018 09:00
End of BL transport		06.06.2017 20:00	01.06.2018 21:00	13.09.2018 09:00	08.10.2018 15:00
Bedload mass	to	748	285	802	280
Bedload volume	m^3	282	107.5	303	106

Bedload mass rate	kg/s	34.6	7.92	18.6	13
Bedload volume rate	m^3/s	0.013	0.003	0.007	0.005
Duration of BL transport (t_{BL})	h	6	10	12	6
Q_{mean} SBT during BL transp. (Q_{BL})	m^3/s	82	59	33	24
Q_{mean} SBT during rain event	m^3/s	71	65	32	31
Mean flow depth (H_{BL})	m	2.0	1.6	1.0	0.8
Mean flow velocity (U_{BL})	m/s	9.4	8.5	7.2	6.5
Froude (F_{BL})	-	2.1	2.2	2.2	2.2
Bed shear stress ($U^*_{BL}=\sqrt{(g^*R_h^*J_s)}$)	m/s	0.441	0.413	0.364	0.337
Slope SBT	-		0.019		
d_{90}	m		0.15		
d_{30}	m		0.015		
d_m	m		0.06		

Table 25: Characteristics of major rain events and SBT operation in 2019 and 2020 at Solis SBT.

		05.06.2019	12.06.2019	12.08.2019	29.08.2020
Start of BL transport		05.06.2019 07:00	12.06.2019 05:00	12.08.2019 20:00	29.08.2020 09:00
End of BL transport		06.06.2019 17:00	16.06.2019 21:00	12.08.2019 22:00	31.08.2020 06:00
Bedload mass	to	8'742	50'616	14	7'423
Bedload volume	m^3	3'299	19'100	5.3	2'801
Bedload mass rate	kg/s	74.4	125.5	1.94	45.82
Bedload volume rate	m^3/s	0.027	0.047	0.0007	0.0173
Duration of BL transport (t_{BL})	h	34	112	2	45
Q_{mean} SBT during BL transp. (Q_{BL})	m^3/s	105	130	23	97
Q_{mean} SBT during rain event	m^3/s	93	130	61	89
Mean flow depth (H_{BL})	m	2.4	2.8	0.8	2.2
Mean flow velocity (U_{BL})	m/s	10.0	10.6	6.4	9.8
Froude (F_{BL})	-	2.1	2.0	2.2	2.1
Bed shear stress ($U^*_{BL}=\sqrt{(g^*R_h^*J_s)}$)	m/s	0.462	0.479	0.334	0.455
Slope SBT	-		0.019		
d_{90}	m		0.15		
d_{30}	m		0.015		
d_m	m		0.06		